Spatial Single-Cell Mapping of Transcriptional Differences Across Genetic Backgrounds in Mouse Brains

Zachary Hemminger[1,2*], Gabriela Sanchez-Tam[2*], Haley De Ocampo[2], Aihui Wang[2], Thomas Underwood[2], Fangming Xie[3], Qiuying Zhao[4], Dongyuan Song[5], Jingyi Jessica Li[6,7], Hongwei Dong[4], Roy Wollman[2,7,8,†]

1. Biocartography Inc.
2. Department of Chemistry and Biochemistry, UCLA
3. Department of Chemical Biology, David Geffen School of Medicine at UCLA
4. Department of Neurobiology, David Geffen School of Medicine at UCLA
5. Independent Program in Bioinformatics, UCLA
6. Department of Statistics and Data Science, UCLA
7. Institute of Quantitative Biosciences, UCLA
8. Department of Integrative Biology and Physiology, UCLA

* Equal contributors.
† Corresponding author.

Abstract

Genetic variation can alter brain structure and, consequently, function. Comparative statistical analysis of mouse brains across genetic backgrounds requires spatial, single-cell, atlas-scale data, in replicates—a challenge for current technologies. We introduce **A**tlas-scale **T**ranscriptome **L**ocalization using **A**ggregate **S**ignatures (ATLAS), a scalable tissue mapping method. ATLAS learns transcriptional signatures from scRNAseq data, encodes them *in situ* with tens of thousands of oligonucleotide probes, and decodes them to infer cell types and imputed transcriptomes. We validated ATLAS by comparing its cell type inferences with direct MERFISH measurements of marker genes and quantitative comparisons to four other technologies. Using ATLAS, we mapped the central brains of five male and five female C57BL/6J (B6) mice and five male BTBR T+ tf/J (BTBR) mice, an idiopathic model of autism, collectively profiling over 40 million cells across over 400 coronal sections. Our analysis revealed over 40 significant differences in cell type distributions and identified 16 regional composition changes across male-female and B6-BTBR comparisons. ATLAS thus enables systematic comparative studies, facilitating organ-level structure-function analysis of disease models.

Main

The quest to link genotype to phenotype is a cornerstone of biology[1]. Advances in molecular mapping now allow for the measurement of complex phenotypes, such as the spatial organization of cellular transcriptional states in organs[2]. Mapping multiple genetic backgrounds will deepen our understanding of how genetics shape organ structure, especially for neurodevelopmental conditions like autism, which have strong genetic underpinnings[3]. However, atlas creation remains limited to single genetic backgrounds or individual animals due to cost and resource constraints[4,5], restricting our understanding of how genetic variation impacts organ architecture. Just as genome sequencing became more feasible with the availability of reference genomes, the availability of spatial reference atlases now enables the development of higher throughput approaches for systematic exploration of the relationship between genetics, anatomy, and physiology.

Spatial transcriptomics is the core technology for organ mapping[2,6], but its ability to capture all RNA molecules is inherently limited. The ease of mapping nucleic acids and the wealth of information the transcriptome provides about cellular phenotypes[7] have made spatial transcriptomics the leading method for organ-wide studies. However, given the enormous number of mRNA molecules—ranging from 10^{16} in large human organs like the liver or brain to 10^{13} in smaller organs like the mouse brain—counting every mRNA molecule is impractical, even when only a subset of an organ is mapped via sectioning. Fortunately, capturing all mRNA molecules is unnecessary. The transcriptome is highly redundant, and most spatial transcriptomic technologies capture less than 1% of total mRNA, relying on computational methods to integrate this data with scRNAseq to build comprehensive atlases. These integration methods have evolved significantly over the past decade, from simple landmark gene approaches[8,9] to advanced computational techniques that harmonize scRNAseq and spatial data[10]. Current mouse brain atlases, built with spatial barcoding[11], in situ sequencing[12], and hybridization methods[4,5], rely on these techniques to create detailed maps.

Given that transcript-level spatial transcriptomics data serves as signatures for data integration, we explored whether more efficient methods could yield more informative signatures. Single-cell transcriptomics tools often reduce the dimensionality of sparse, high-dimensional transcriptomes using techniques like principal component analysis (PCA)[13] or non-negative matrix factorization (NMF)[14], demonstrating that these reduced-dimensional approximations of transcriptional states serve as powerful signatures for scRNAseq data integration. Currently,

such signatures are accessible only in silico, requiring laborious RNA counting. Could these transcriptional signatures be measured directly, bypassing the need for individual gene expression measurements? Aggregate measurements, where multiple genes are measured together, have been used for compressed sensing[15] and to enhance fluorescence detection sensitivity[16]. We realized that, with the appropriate design of an oligonucleotide probe pool, aggregate measurements could directly encode lower-dimensional cellular transcriptional signatures in situ. This approach enables the direct measurement of transcriptional states without counting individual RNA molecules. It allows us to measure transcriptional signatures at the cell level, making ATLAS suitable for large-scale measurements and facilitating comprehensive organ mapping.

Here, we introduce ATLAS, a scalable tissue mapping technology that combines in situ encoding, based on existing reference atlas data (Figure 1), with in silico decoding to generate cell type maps and imputed transcriptomes (Figure 2). We validated ATLAS by directly measuring marker genes in ATLAS samples and conducting quantitative comparisons with reference atlas data (Figure 2). To demonstrate its scalability, we performed comparative studies of sex dimorphism in B6 mice and a comparison between male B6 and BTBR animals, an autism model. We mapped the central brain region (CCFx 4.5-9.5 mm) using 21–49 coronal sections per brain. ATLAS produced detailed cell type maps and imputed transcriptomes for over 40 million cells from 405 sections across 15 animals. Using these data, we reconstructed 3D cell type distributions across the three conditions (Figure 3). Two complementary comparative analyses were conducted: first, identifying cell types with statistically significant differences in spatial distribution—two in the male-female comparison and 41 in the B6-BTBR comparison (Figure 4); and second, identifying differences in overall cell type composition, revealing two regions with differences in male-female comparisons and 14 regions in B6-BTBR comparisons (Figure 5). These results demonstrate the power of ATLAS in revealing how genetic variation influences organ architecture.

In situ encoding of cellular transcriptional signatures

ATLAS expands the capabilities of encoding hybridization from binary codes to linear projection. Encoding hybridizations like MERFISH[17] and seqFISH[18] rely on binary bipartite codebook matrices, where each matrix element b_{ij} represents the mapping between gene *i* and readout *j*, achieved using pools of bivalent DNA oligos that bind both the gene and the readout. To extend beyond binary mappings, we designed oligo pools to represent continuous weights w_{ij}, where each weight corresponds to the number of probes per gene *i* for a given readout *j*, allowing hybridization to perform a matrix multiplication of a nonnegative weight matrix with a cellular transcriptome vector. This enables the projection of cellular mRNA into a low-dimensional space *in situ* (Figure 1b). We implemented this using DPNMF, a variant of non-negative matrix factorization[19,20], which reconstructs gene expression data while separating predefined labels, producing sparse, low-dimensional factorizations. Using BICCN single-cell transcriptional data and cell-type labels[21], we derived a DPNMF projection matrix that reduces 6,133 genes into an 18-dimensional transcriptional signature. The matrix was scaled and digitized to match the number of encoding probes binding sites available. DPNMF's sparsity made this feasible with a total of 31,564 probes in the final oligo pool, enabling efficient *in situ* implementation of a dimensionality reduction operation.

To ensure that *in situ* measurements accurately reflected the designed linear projections, we optimized the protocol to minimize non-specific binding and eliminate non-specific signals. Building on the MERFISH protocol [22], we made several adjustments (see Methods). Key changes included: (1) Clearing twice, before and after encoder probe hybridization; (2) RNA encoder probes with higher melting temperatures than DNA, allowing them to stay bound during high-temperature clearing and enable more stringent hybridization with DNA readout probes (Extended Figure 2ab); (3) Enhanced mRNA anchoring to polyacrylamide gels using melpha-X [23], ensuring RNA retention during clearing (Extended Figure 2c); and (4) Acquisition of background images before each hybridization round for accurate subtraction of residual fluorescence (Extended Figure 2d). These optimizations enabled us to reliably use total integrated fluorescent intensity to measure cellular transcriptional signatures.

We then stained a brain section with DPNMF probes and measured the projection of cellular transcriptional states (Figure 1c). The resulting data revealed distinct transcriptional states across different cells, which produced brain regions with clear spatial signatures. Some projected components displayed multimodal distributions, while others exhibited more continuous patterns, indicating multiple distinct subpopulations (Extended Figure 3a) providing an insight into DPNMF encoding. Specific regions, such as the cortical layers, demonstrated clear combinatorial encoding of transcriptional states (Figure 1d). These results show that our encoding approach captures rich and diverse information about cellular transcriptional states.

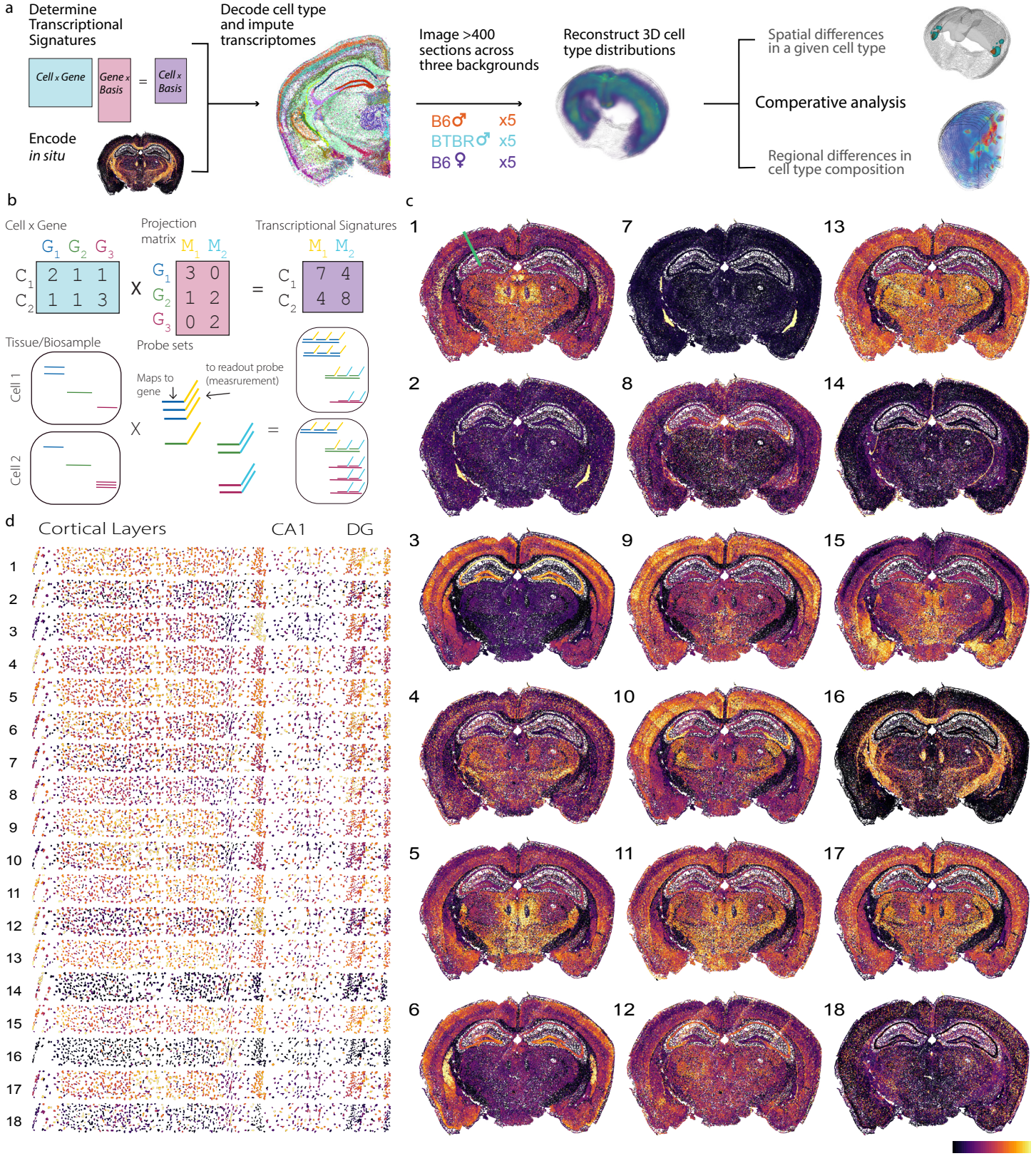

Figure 1. Encoding cellular transcriptional state using ATLAS. (a) Overview of the ATLAS pipeline. (b) Comparison of *in silico* (top row) and *in situ* (bottom row) encoding. The projection matrix, derived from scRNAseq data, is implemented *in situ* by matching the weights of w_{ij} to the number of encoding probes in the oligonucleotide pool. Hybridization effectively performs non-negative matrix multiplication. (c) Encoded transcriptional signatures from a single coronal mouse brain section. The green line in (c-1) indicates the region shown at higher magnification in (d), extending from the cortical layer to the dentate gyrus (DG). The colorbar scale is independent for each panel, with colors representing relative intensity differences specific to each panel.

Decoding and validation of ATLAS signatures

The aggregate signatures represent a dimensionality-reduced version of cellular transcriptional states, making them suitable for direct use in unsupervised clustering. Using standard Leiden clustering on a correlation-based KNN graph of cells (see Methods), we identified distinct clusters that qualitatively align with known brain regions, supporting the notion that ATLAS signatures are highly informative and provide insights into underlying cellular transcriptional states (Extended Figure 3b). This demonstrates the strength of using dimensionality-reduced representations for classifying cells, especially in cases where no agreed-upon cell type taxonomy exists. However, continuously generating new cell type taxonomies with each brain mapping effort is impractical and adds confusion within the research community, as it necessitates mapping across different nomenclatures [24]. To address this challenge within the ATLAS framework, we developed a complementary supervised approach that aligns ATLAS's decoding with existing reference nomenclature, reducing confusion across studies.

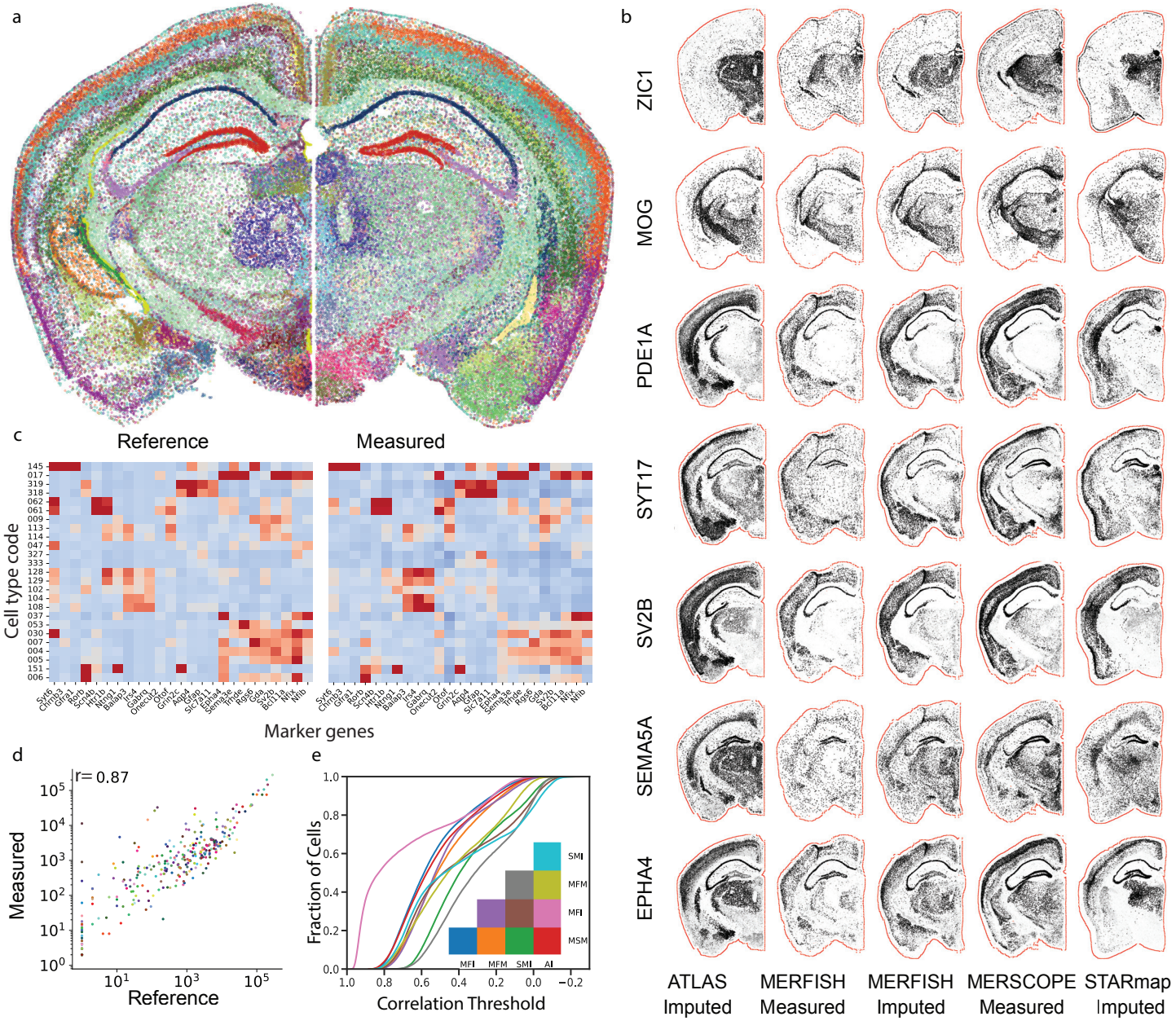

Figure 2. Decoding of ATLAS transcriptional signatures. (a) Comparison between cell types identified using MERFISH gene expression signatures in the reference atlas (left) and cell types inferred from ATLAS transcriptional signatures (right). Cell are colored based on the reference atlas subclass color scheme (b) Representative gene expression plots for seven genes measured across five platforms on matched sections. (c) Comparison of the 25 most abundant cell types, showing reference average expression of marker genes and a validation dataset where cell types were inferred from low-magnification ATLAS imaging, with gene expression measured using MERFISH on the same sample. (d) Total abundance of cell types in the central brain, comparing reference data to ATLAS-inferred data, with the Pearson correlation coefficient (r = 0.87) shown. (e) Quantification of agreement between technologies: for each pair of technologies (color-coded), cumulative probability distributions of gene expression correlation (across 336 genes) are plotted for synthetically paired cells between the technologies (see Methods).

To decode ATLAS signatures into predefined cell types, we developed a Bayesian recursive harmonization and classification approach called SCALE (Single Cell Alignment Leveraging Existing data, Extended Figure 4a, see Methods for details). The Bayesian framework was chosen for two key reasons: (1) it maximizes the use of reference atlas information, consistent with the principles of ATLAS, and (2) it leverages strong prior knowledge of cell type distributions based on anatomical location in the brain. We generated spatial probability maps for each cell type subclass and incorporated supervised learning based on reference scRNAseq data to infer the posterior probability of a transcriptional signature belonging to a specific cell type. The process involved projecting scRNAseq data into a lower-dimensional space and harmonizing it with ATLAS data through a recursive classification and correction approach. Following the strategy used to harmonize reference atlas FISH with scRNAseq data [4], we stepped through the cell-type dendrogram, applying simple linear corrections after each classification step (Extended Figure 4ac). This recursive descent brought the ATLAS data into the projected scRNAseq reference space, making imputation a straightforward process using a KNN approach. The final cell-type calls qualitatively matched expected data (Figure 2b).

To validate ATLAS, we employed two complementary approaches: direct measurement of marker genes and quantitative comparison to existing reference atlases. Marker genes were measured following a modified MERFISH protocol, where cellular mRNAs were anchored to a polyacrylamide gel (see Methods). After imaging, the MERFISH probes were removed using denaturing conditions, and the same sample was hybridized with ATLAS RNA encoding probes. Because the tissue mRNAs were covalently anchored to the gel, we experienced minimal RNA loss, allowing repeated imaging with both protocols. Using this procedure, we measured the expression of 170 marker genes, a subset of the original set used in the reference atlas [4], for cells in a single coronal section hemisphere, and obtained their cell type information using ATLAS encoding/decoding. We found remarkable agreement between the reference and ATLAS-decoded marker genes for all cell types, qualitatively validating ATLAS decoding (Figure 2c). Initial quantification showed a strong correlation in cell type abundance between ATLAS and reference data (Pearson correlation of 0.87). However, this does not account for spatial positioning. To quantitatively assess spatial predictions, we compared ATLAS to multiple reference datasets, as none represent a definitive biological 'ground truth.' We developed a statistical pairing procedure using a greedy algorithm to optimize correlation scores and spatial proximity (see Methods), generating a distribution of correlation values for each cell pair across 336 shared genes (Figure 2e). ATLAS imputation showed comparable agreement with MERSCOPE and MERFISH atlases, similar to the agreement between these two independently measured datasets. StarMAP, which uses in situ sequencing and a different scRNAseq dataset for imputation, had the lowest agreement with other methods. Notably, the strongest agreement was observed between ATLAS and MERFISH imputation, demonstrating that 18-dimensional cellular-level transcriptional signatures can be as effective as 1100-dimensional gene-level signatures for imputation purposes. These validation analyses confirm that ATLAS provides accurate cell type inference and gene expression imputation.

Scaling acquisition to map 15 mouse brains

Encouraged by the high quality of the ATLAS signatures, we expanded the scale of data collection. Iterative FISH approaches rely on high-magnification imaging and a closed chamber design, imaging one coverslip at a time. To fully leverage ATLAS' capabilities for large-area imaging with low magnification, we redesigned the fluidics system to use an open chamber design (Extended Figure 5). This allowed for multi-well imaging, where three wells were hybridized while the other three were imaged, enabling continuous imaging and minimizing the impact of hybridization time. We also used large 40 mm coverslips in each of the six wells, accommodating four coronal brain sections per coverslip. A single 3-day imaging run thus captures data from 24 brain sections. Data were collected from 15 brains across three conditions (B6 female, B6 male, BTBR male). Initially, each brain was sectioned into 24 serial sections, spaced 200 μm apart, covering CCFx from 4.5 to 9.5 mm. The 20 μm-thick sections were taken in triplicate, allowing us to replace sections that did not meet quality standards (see methods). For instance, brain WTM05 required three imaging runs due to section failures in the first two, ultimately resulting in 49 sections for this brain. After quality control (see methods), the dataset comprised over 40 million cells from over 400 sections (Figure 3a, Extended Figure 6).

This large dataset was then used to construct 3D spatial distribution maps for all 334 cell types at the subclass level across the three mapped conditions (Figure 3c, see Methods for details). In constructing these surfaces, we assumed left-right brain symmetry, effectively increasing the sample size from five to ten per condition. This larger sample size helped address missing values, primarily caused by sectioning artifacts such as tears, folds, etc. Focusing on subclass granularity, we created volumetric estimates of the spatial abundance for each cell type using 100 μm^3 voxels. All statistical comparisons between conditions employed a permutation strategy,

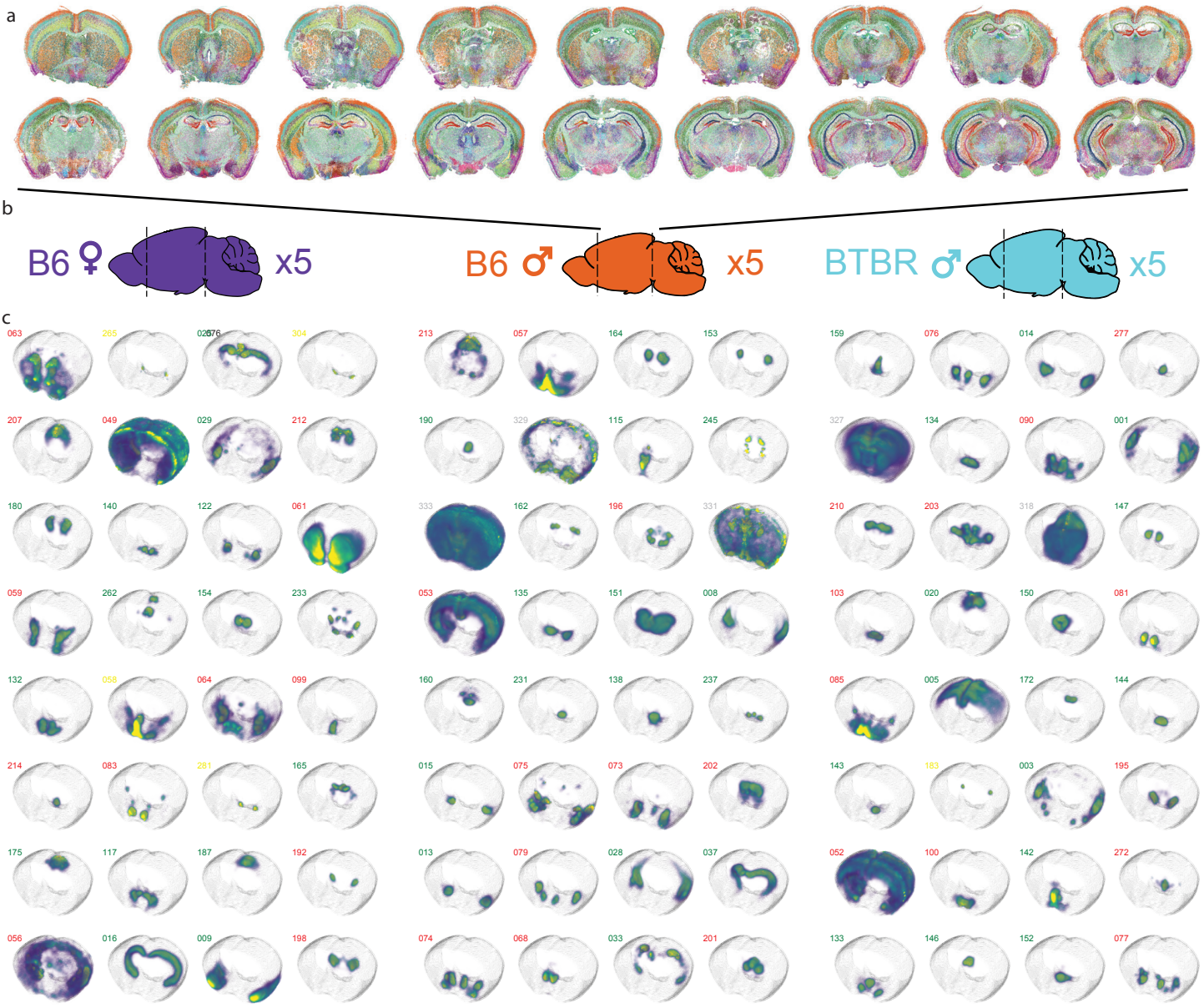

Figure 3. Inference of 3D cell type distributions across B6-female, B6-male, and BTBR-male conditions. (a) Representative 18 serial sections from a single animal, with cell types color-coded based on the reference atlas subclass color scheme. (b) The dataset includes brains from 15 animals, sectioned from CCFx 4.5 to CCFx 9.5, with an average of 27 sections per animal (range: 21–49). (c) Spatial distributions of all 334 cell subclass types were inferred for each condition. Shown are 32 representative cell types per condition. Cell type codes are shown above each distribution color-coded as follows: red (GABA neurons), green (Glutamatergic neurons), yellow (other neurons), and gray (non-neuronal cells). For visualization, different cell types are displayed for each condition, although all 334 types were inferred for all conditions.

where animal labels were permuted, and hundreds of thousands of volumetric cell-type spatial abundances were inferred under the null hypothesis that there are no differences between genetic backgrounds.

Differences in spatial distribution at the cell type level

Building on the accuracy (Figure 2) and scale (Figure 3) of our cell-type volumetric maps, we conducted a comparative analysis to identify differences in spatial distributions across B6 male vs. female and B6 male vs. BTBR male. We focused on the spatial distribution of each of the 334 subclasses across the two conditions (see Methods). To ensure that our analysis captured spatially explicit differences, we first calculated for each voxel, the difference (residual) between the two conditions. We then quantified the overall spread of residual distribution using entropy measure. This approach quantifies the divergence between spatial distributions while maintaining spatial context, where lower entropy indicates greater similarity and higher entropy reflects more pronounced differences. Statistical significance was assessed by comparing the observed entropy values to a null distribution generated through permutation. Permutation was performed on the animal label, and the resulting p-values were adjusted for multiple hypothesis testing using the false discovery rate (FDR).

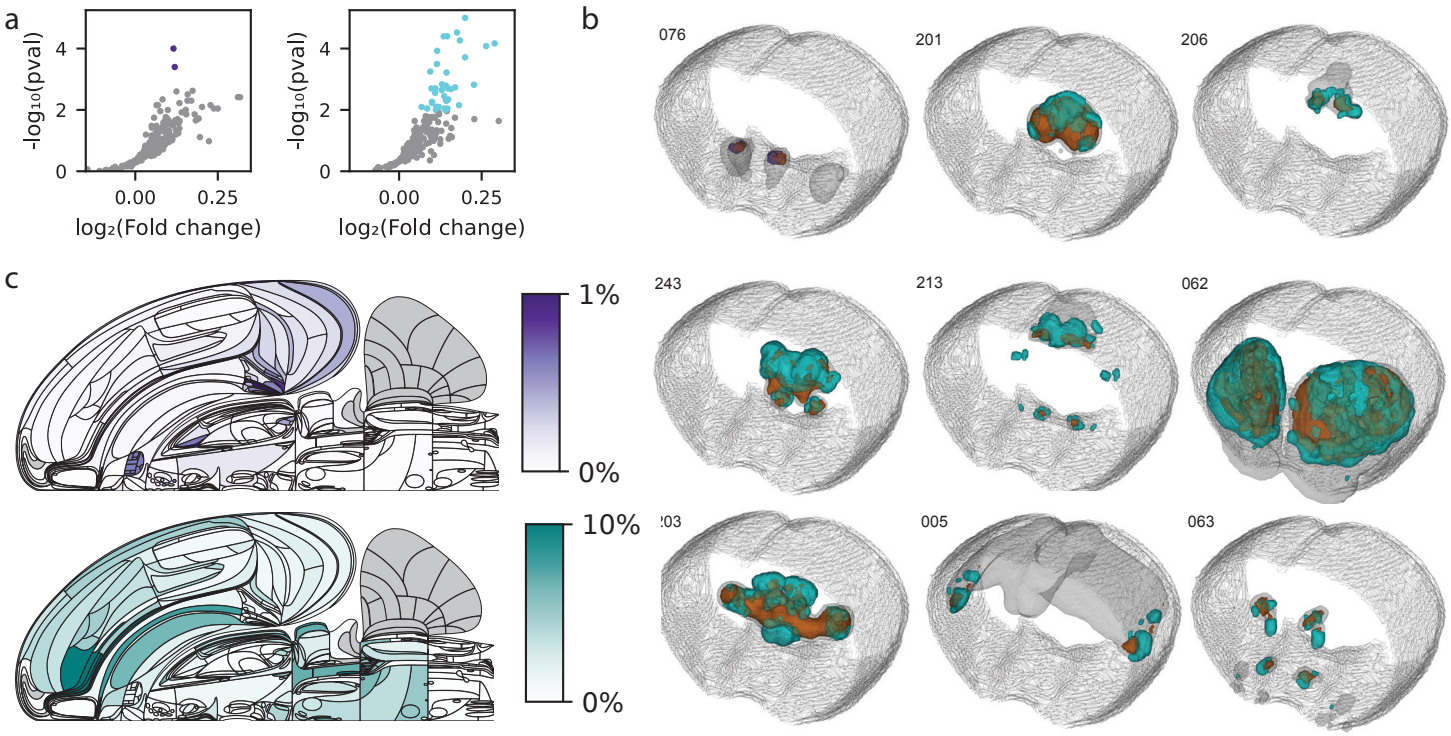

Figure 4 | Spatial differences in cell type distribution across male-female and B6-BTBR comparisons. (a) Volcano plots illustrating effect size versus significance from the statistical permutation test (see Methods) for all 334 cell types at the subclass level. The comparison between B6 males and B6 females (left) identified two cell types with significant spatial distribution differences, while the B6-BTBR comparison (right) identified 41 cell types. (b) Nine representative cell types with significant spatial distribution differences. The overall volume occupied by each cell type across conditions is shown in gray, with areas of increased levels in B6 males, B6 females, or BTBR animals highlighted in orange, purple, and cyan, respectively. Shown (left to right, top to bottom) are: 076_MEA-BST_Lhx6_Nfib_Gaba, 201_PAG-RN_Nkx2-2_Otx1_Gaba, 206_SCm-PAG_Cdh23_Gaba, 243_PGRN-PARN-MDRN_Hoxb5_Glut, 213_SCsg_Gabrr2_Gaba, 062_STR_D2_Gaba, 203_LGv-SPFp-SPFm_Nkx2-2_Tcf7l2_Gaba, 005_L5_IT_CTX_Glut, and 063_STR_D1_Sema5a_Gaba. (c) Flatmap representation quantifying the number of cell type changes in each brain region, shown as a weighted fraction of the total number of cell types in the region, adjusted by cell type abundance. Colorbar shows the fraction of total differences over total cells for each brain region summed over all cell types. The top map shows the male-female comparison, while the bottom map shows the B6-BTBR comparison.

The male-female comparison revealed significant spatial differences in two GABAergic neuron types (Figure 4a, Supplementary Table 1). The first, '076 MEA-BST Lhx6 Nfib Gaba,' aligns with neuronal populations previously linked to male social behaviors [24,25]. The second, '050 Lamp5 Lhx6 Gaba,' had not been previously implicated in sexual dimorphism, yet expresses markers associated with neurons from the sexually dimorphic preoptic area (POA) [24], a region known to regulate sex-specific brain function [26]. Analyzing the magnitude and spatial distribution of these differences (Figure 4c), we found that they are localized to the hypothalamus and affect up to ~1% of neurons in regions such as the medial amygdala (MEA), indicating a modest but regionally specific impact.

The B6-BTBR comparison revealed 41 significant differences in cell type distributions, affecting a larger number of brain regions and showing greater magnitude than the male-female comparison (Figure 4ab). These differences included both inhibitory and excitatory neuron subclasses. Notably, changes were enriched in the Agranular Insular cortex (AIv and AId), with overall differences in neuronal populations exceeding 10% in these regions. Previous studies have also identified the insular cortex as a key region of difference in BTBR animals [27,28], where altered cell type composition is thought to affect multisensory integration compared to B6 mice. Another region showing over 10% change was the dorsal raphe nucleus (DR), in agreement with prior studies using broader cell type inference from antibody staining [29].

These findings underscore the strengths of ATLAS in comparative spatial distribution analysis, revealing both well-characterized and previously unexplored differences in cell type spatial distributions. The high granularity of transcriptionally defined neuron types provided more detailed insights than prior histopathological studies, which reported only modest differences between B6 and BTBR brains [30]. However, using high-granularity cell types as a comparison unit poses challenges: (1) molecular changes within a cell type may not significantly alter its transcriptional state enough to change 'type identity,' and (2) localized shifts in cell type distribution may be

difficult to detect when most of the cell type remains spatially consistent. While the first challenge is intrinsic to ATLAS and requires further data, the second could be addressed through complementary analysis that compares spatial distributions on a voxel level rather than by cell type.

Regional differences in cell type composition

The composition of cell types across brain regions plays a key role in shaping brain function. To assess local and regional differences in cell type composition for the male-female and B6-BTBR comparisons, we calculated the voxel-wise correlation distance of cell type composition vectors between the two conditions. These correlation distances were compared to a null distribution generated by permuting animal labels, resulting in a 3D probabilistic map that highlights spatial locations where differences between conditions are unlikely to arise by chance (Figure 5).

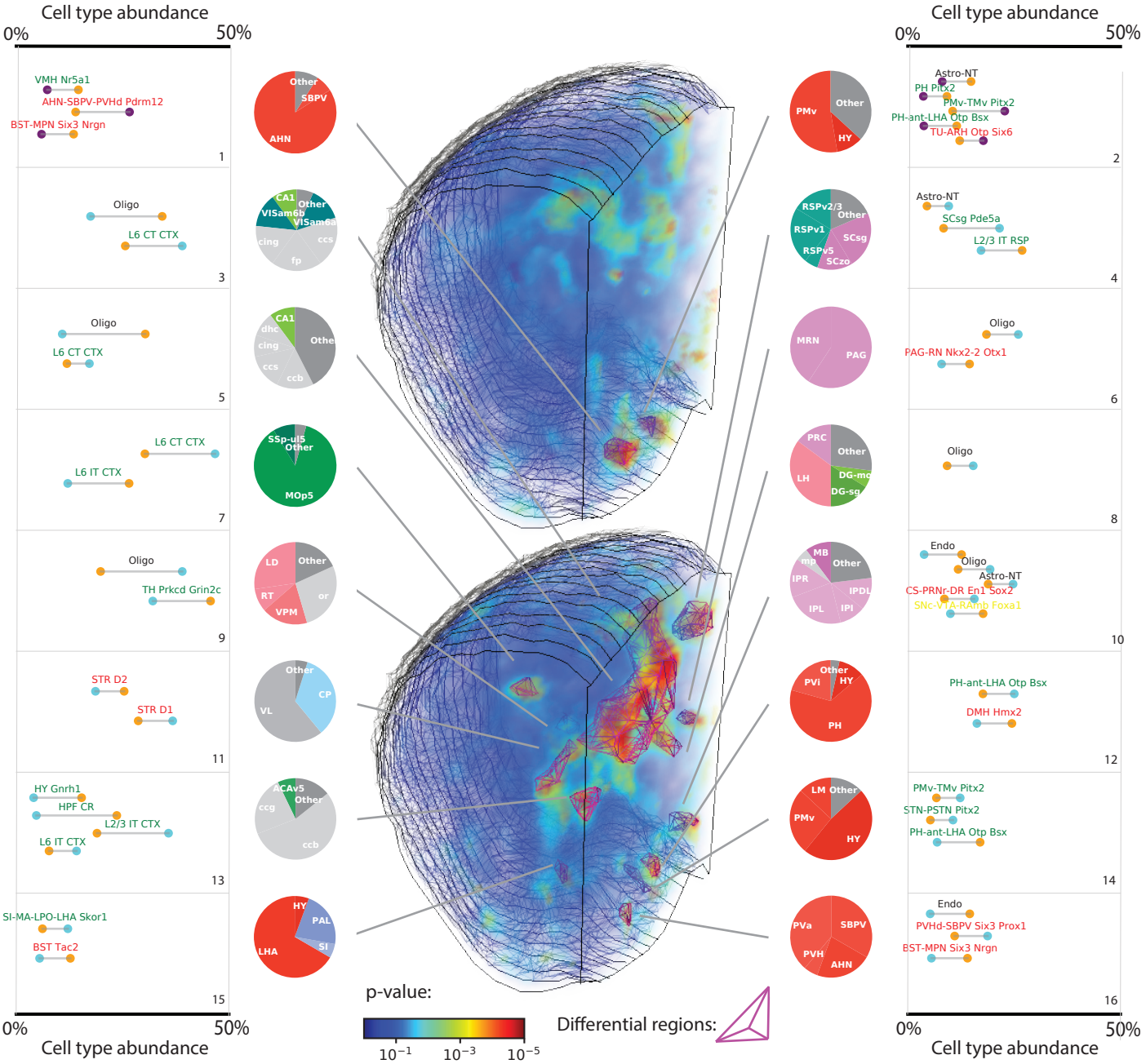

Figure 5. Spatial differences in regional composition across male-female and B6-BTBR comparisons. Volumetric maps show p-values for each spatial position, indicating the likelihood that cell type composition in B6 females (top) or BTBR males (bottom) differs from B6 males, based on permutation testing. Differential regions were defined as continuous areas larger than 0.015 mm^3 with voxel p-values ≤ 0.0002. Two differential regions were identified in the B6 male versus B6 female comparison, while 14 regions were identified in the B6 versus BTBR comparison. For each region, pie charts show the magnitude of overlap between each differential region and known brain areas; acronyms and color codes follow the CCF atlas. Outer panels of each pie chart display cell types in each differential region with >5% abundance difference. Dots represent cell types colored by condition: orange (B6 male), purple (B6 female), and cyan (BTBR). Gray lines indicate the magnitude of abundance differences.

We identified two adjacent regions within the hypothalamus that exhibited significant sexual dimorphism. Region 1 overlaps with the anterior hypothalamic nucleus (AHN), while Region 2 primarily overlaps with the ventral premammillary nucleus (PMv). Both regions are known to be sexually dimorphic[31], though they have been studied to different extents. Interestingly, the AHN was one of the first sexually dimorphic regions identified in rats in 1977 [32] and was initially believed to be similar across mammals. However, follow-up studies showed that, unlike in rats, there are no morphological differences in the AHN of mice[33]. More recent molecular studies have re-established its sexually dimorphic nature[34], and our findings of specific neuronal cell type differences further refine the molecular resolution of sexual dimorphism in the AHN. Region 2, the PMv, is a well-established sexually dimorphic region, with roles in maternal aggression[35], reproductive control[36], male social behavior[37], and intermale aggression[38]. Previous studies identified sexually dimorphic neuron populations within the PMv (e.g., PMv-DAT[39], PMv-PACAP[40]), complementing our systematic identification of subclass-level abundance changes. Interestingly, although we identified several neurons associated with the ventromedial hypothalamus (VMH), a known sexually dimorphic region located between the AHN and PMv, the VMH itself did not show significant differences (p-value = 0.08). Interpreting such negative results is challenging as it could simply be that we do not have the statistical power to find differences and further analysis using the high throughput capabilities of ATLAS may clarify this. It is also possible that sexual dimorphism in the VMH is driven more by gene expression or chromatin state changes than by cell type abundance, an open question in many sexually dimorphic brain regions[41].

We identified 14 regions with distinct cell type compositions in BTBR males compared to B6 males. Regions 3 and 5 showed a marked decrease in oligodendrocytes in BTBR mice, alongside a mild increase in cortical neurons. This aligns with the BTBR model's lack of a corpus callosum [30], a region typically enriched in oligodendrocytes. These regions also overlapped with areas with high morphological difference from the CCF reference (Extended Figure 7). Region 13 also overlaps with fiber tracts, but instead of an increase in oligodendrocytes, we observed a notable rise in HPF CR neurons. In contrast, Regions 6, 8, 9, and 10 exhibited higher numbers of oligodendrocytes in BTBR mice, accompanied by reductions in PAG-RN Nkx2-2 Otx1 GABAergic neurons in Region 6, and decreases in TH Prkcd Grin2c glutamatergic neurons in Region 9, along with multiple cell type changes in Regions 8 and 10. Region 4 overlaps with the retrosplenial cortex, which has been shown to have reduced volume in BTBR mice via fMRI, though molecular details were lacking [42]. Regions 12, 14, 15, and 16 overlap with various hypothalamic nuclei, and across these regions, more than 10 cell types showed over 5% compositional differences. Regions 7 and 11 were dominated by a switch between two closely related cell types (L6 CT CTX to L6 IT CTX in Region 7, and STR D1 to STR D6 in Region 11). Given that the underlying transcriptional changes in these cells are more continuous than implied by these discrete labels, it is likely that the differences in these regions reflect more gradual transcriptional shifts, which are captured as compositional changes in our analysis that places cells into distinct categories.

These findings demonstrate ATLAS's capability to perform large-scale comparative compositional analyses across spatial volumes exceeding 400 mm^3, with voxel sizes of 0.001 mm^3, each containing tens of cells. Many of the regions identified as compositionally different were previously associated with sexual dimorphism or behavioral differences between B6 and BTBR mice, while other regions are novel. Further investigation is required to elucidate the functional implications of these newly identified changes in cellular composition across these regions.

Discussion

ATLAS is a scalable approach for mapping cellular transcriptional states by learning transcriptional signatures from reference scRNAseq data, encoding them in situ with oligo pools, and decoding them to infer cell types and imputed transcriptomes. By incorporating data integration from the outset, ATLAS optimizes tissue mapping by eliminating the need to measure individual genes, relying instead on transcriptional signatures derived from matrix factorization. We validated ATLAS's accuracy through direct measurements of marker genes and quantitative comparison with four other brain atlases, demonstrating its performance to be on par with or better than traditional gene expression reconstruction methods. ATLAS's high throughput, as demonstrated by profiling over 40 million cells across 15 animals, enabled in-depth comparative analyses that revealed significant differences in cell-type spatial distributions and regional composition across the brain. In the male-female comparison, ATLAS identified differences in two GABAergic neuron types and highlighted sexually dimorphic regions such as the anterior hypothalamic nucleus (AHN) and the ventral premammillary nucleus (PMv), both linked to sex-specific behaviors. In the B6-BTBR comparison, ATLAS uncovered 41 distinct cell types with spatial distribution differences and regional changes across 14 brain regions, including reductions in oligodendrocytes and increases in cortical

neurons in the Agranular Insular cortex and dorsal raphe nucleus, regions previously associated with autism-related behaviors. Crucially, ATLAS not only confirmed established differences but also uncovered novel regions and cell type variations, generating key hypotheses about molecular neuroanatomical differences underlying functional variations between genetic backgrounds. This demonstrates the power of ATLAS as a comprehensive tool for systematic tissue mapping and comparative studies of brain structure-function relationships.

ATLAS's scalability arises from its shift from single-molecule to single-cell imaging, resulting in ~100x faster imaging and ~100x smaller image datasets, simplifying downstream computational analysis. Importantly, this benefit comes without a reduction in accuracy. However, there are downsides to transitioning from molecule-level to cell-level transcriptional signatures. First, ATLAS lacks subcellular resolution. While this can be addressed by combining ATLAS with MERFISH to capture submicron gene expression data, doing so reintroduces molecule-level measurements, counteracting ATLAS's key advantages. Second, ATLAS requires high-quality scRNAseq reference data. Although the decreasing cost of scRNAseq and the growing availability of reference datasets mitigate this issue in most cases, challenges remain when mapping nontraditional model organisms or disease conditions with heavily perturbed transcriptional states, where generating new reference data would increase overall costs. Third, ATLAS completely relies on data integration with scRNAseq. While gene-level transcriptional signatures also benefit from data integration, they can still be interpreted directly without it. ATLAS's deep reliance on data integration is both its greatest advantage—enabling its substantial scalability—and its most significant limitation, as it makes the method more indirect. This trade-off ensures that there will always be a role for approaches providing direct gene expression measurements.

Several avenues exist for improving ATLAS. First, the reference dataset used to design the encoding scheme was outdated and only included scRNAseq data from the cortex and hippocampus [21]. The fact that this encoding performed well across other brain regions highlights the robustness of our approach, but updating the reference data would further enhance ATLAS's accuracy. Second, in this study, we chose to use 18-dimensional transcriptional signatures. This choice represents a tradeoff between accuracy and throughput, and future applications of ATLAS should adjust this hyperparameter to balance throughput needs and decoding complexity. Third, ATLAS's throughput could be significantly increased through signal amplification methods, reducing imaging times and potentially eliminating the need to capture background signals, which could cut imaging time in half. However, the amplification must be linear to preserve the accurate representation of cellular transcriptional states—a requirement that does not apply to transcript-level measurements. This limits the use of non-linear amplification methods like RCA [43], but both bDNA [44] and HCR [45] offer promising avenues for linear amplification, potentially boosting throughput by another 10x. Fourth, the polyacrylamide RNA anchoring and extensive clearing used in ATLAS make it compatible with light sheet imaging, which could further increase throughput and enable 3D reconstruction of entire organs. Finally, while this study focused on cell type-related gene expression programs, ATLAS could be adapted to map any gene expression program involving multiple genes—such as those related to inflammation, cancer, or stress—by incorporating additional aggregate signatures, thereby providing cellular insights beyond cell type identity.

Databases like the Protein Data Bank (PDB) have been essential in understanding the structure-function relationship at the molecular level, often through comparisons of wild-type and mutated protein structures. Similarly, ATLAS offers a way to reconstruct anatomical structures at single-cell resolution across conditions with known genetic and functional differences. This paves the way for the creation of an 'Organ Data Bank,' analogous to the PDB, that would enable systematic analysis of the relationship between organ structure (anatomy) and function (physiology).

Data and code availability

All data is available here (https://doi.org/10.5281/zenodo.13851748) and code can be found here (ATLAS https://github.com/wollmanlab/ATLAS_Mouse_Brain/ MERFISH https://github.com/wollmanlab/PySpots Imaging https://github.com/wollmanlab/Scope Fluidics https://github.com/wollmanlab/Fluidics)

Acknowledgements

This project was supported by NIH grant R01-HG012925.

Ethical statement

ZH and RW are the co-founders of Biocartography Inc.

References

1. Johannsen, W. The genotype conception of heredity. *Am. Nat.* **45**, 129–159 (1911).
2. Moffitt, J. R., Lundberg, E. & Heyn, H. The emerging landscape of spatial profiling technologies. *Nat. Rev. Genet.* (2022) doi:10.1038/s41576-022-00515-3.
3. Ramaswami, G. & Geschwind, D. H. Genetics of autism spectrum disorder. *Handb. Clin. Neurol.* **147**, 321–329 (2018).
4. Yao, Z. *et al.* A high-resolution transcriptomic and spatial atlas of cell types in the whole mouse brain. *Nature* **624**, 317–332 (2023).
5. Zhang, M. *et al.* Molecularly defined and spatially resolved cell atlas of the whole mouse brain. *Nature* **624**, 343–354 (2023).
6. Nagle, M. P., Tam, G. S., Maltz, E., Hemminger, Z. & Wollman, R. Bridging scales: From cell biology to physiology using in situ single-cell technologies. *Cell Systems* **12**, 388–400 (2021).
7. Maltz, E. & Wollman, R. Quantifying the phenotypic information in mRNA abundance. *Mol. Syst. Biol.* **18**, e11001 (2022).
8. Satija, R., Farrell, J. A., Gennert, D., Schier, A. F. & Regev, A. Spatial reconstruction of single-cell gene expression data. *Nat. Biotechnol.* **33**, 495–502 (2015).
9. Halpern, K. B. *et al.* Single-cell spatial reconstruction reveals global division of labour in the mammalian liver. *Nature* (2017) doi:10.1038/nature21065.
10. Kleshchevnikov, V. *et al.* Cell2location maps fine-grained cell types in spatial transcriptomics. *Nat. Biotechnol.* **40**, 661–671 (2022).
11. Langlieb, J. *et al.* The molecular cytoarchitecture of the adult mouse brain. *Nature* **624**, 333–342 (2023).
12. Shi, H. *et al.* Spatial atlas of the mouse central nervous system at molecular resolution. *Nature* **622**, 552–561 (2023).
13. Korsunsky, I. *et al.* Fast, sensitive and accurate integration of single-cell data with Harmony. *Nat. Methods* **16**, 1289–1296 (2019).
14. Welch, J. D. *et al.* Single-Cell Multi-omic Integration Compares and Contrasts Features of Brain Cell Identity. *Cell* **177**, 1873–1887.e17 (2019).
15. Cleary, B. *et al.* Compressed sensing for highly efficient imaging transcriptomics. *Nat. Biotechnol.* **39**, 936–942 (2021).
16. Zhou, X. *et al.* Highly sensitive spatial transcriptomics using FISHnCHIPs of multiple co-expressed genes. *Nat. Commun.* **15**, 2342 (2024).
17. Chen, K. H., Boettiger, A. N., Moffitt, J. R., Wang, S. & Zhuang, X. Spatially resolved, highly multiplexed

RNA profiling in single cells. *Science* **348**, aaa6090 (2015).

18. Eng, C.-H. L. *et al.* Transcriptome-scale super-resolved imaging in tissues by RNA seqFISH. *Nature* **568**, 235–239 (2019).
19. Guan, N., Zhang, X., Luo, Z., Tao, D. & Yang, X. Discriminant projective non-negative matrix factorization. *PLoS One* **8**, e83291 (2013).
20. Song, D., Li, K., Hemminger, Z., Wollman, R. & Li, J. J. scPNMF: sparse gene encoding of single cells to facilitate gene selection for targeted gene profiling. *Bioinformatics* **37**, i358–i366 (2021).
21. Yao, Z. *et al.* A taxonomy of transcriptomic cell types across the isocortex and hippocampal formation. *Cell* **184**, 3222–3241.e26 (2021).
22. Moffitt, J. R. & Zhuang, X. Chapter One - RNA Imaging with Multiplexed Error-Robust Fluorescence In Situ Hybridization (MERFISH). in *Methods in Enzymology* (eds. Filonov, G. S. & Jaffrey, S. R.) vol. 572 1–49 (Academic Press, 2016).
23. Wang, Y. *et al.* EASI-FISH for thick tissue defines lateral hypothalamus spatio-molecular organization. *Cell* **184**, 6361–6377.e24 (2021).
24. van Velthoven, C. T. J. *et al.* The transcriptomic and spatial organization of telencephalic GABAergic neuronal types. *bioRxivorg* (2024) doi:10.1101/2024.06.18.599583.
25. Knoedler, J. R. *et al.* A functional cellular framework for sex and estrous cycle-dependent gene expression and behavior. *Cell* **185**, 654–671.e22 (2022).
26. Bayless, D. W. & Shah, N. M. Genetic dissection of neural circuits underlying sexually dimorphic social behaviours. *Philos. Trans. R. Soc. Lond. B Biol. Sci.* **371**, 20150109 (2016).
27. Sato, M., Nakai, N., Fujima, S., Choe, K. Y. & Takumi, T. Social circuits and their dysfunction in autism spectrum disorder. *Mol. Psychiatry* **28**, 3194–3206 (2023).
28. Gogolla, N., Takesian, A. E., Feng, G., Fagiolini, M. & Hensch, T. K. Sensory integration in mouse insular cortex reflects GABA circuit maturation. *Neuron* **83**, 894–905 (2014).
29. Higuchi, Y., Tachigori, S.-I. & Arakawa, H. Faded neural projection from the posterior bed nucleus of the stria terminalis to the lateral habenula contributes to social signaling deficit in male BTBR mice as a mouse model of autism. *Psychoneuroendocrinology* **149**, 106004 (2023).
30. Stephenson, D. T. *et al.* Histopathologic characterization of the BTBR mouse model of autistic-like behavior reveals selective changes in neurodevelopmental proteins and adult hippocampal neurogenesis. *Mol. Autism* **2**, 7 (2011).
31. De Vries, G. J. & Simerly, R. B. Anatomy, development, and function of sexually dimorphic neural circuits in the mammalian brain. in *Hormones, Brain and Behavior* 137–XXIX (Elsevier, 2002).
32. Mathews, D. & Edwards, D. A. Involvement of the ventromedial and anterior hypothalamic nuclei in the

hormonal induction of receptivity in the female rat. *Physiol. Behav.* **19**, 319–326 (1977).

33. Young, J. K. A comparison of hypothalami of rats and mice: lack of gross sexual dimorphism in the mouse. *Brain Res.* **239**, 233–239 (1982).
34. Wolfe, C. A. *et al.* Sex differences in the location of immunochemically defined cell populations in the mouse preoptic area/anterior hypothalamus. *Brain Res. Dev. Brain Res.* **157**, 34–41 (2005).
35. Motta, S. C. *et al.* Ventral premammillary nucleus as a critical sensory relay to the maternal aggression network. *Proc. Natl. Acad. Sci. U. S. A.* **110**, 14438–14443 (2013).
36. Leshan, R. L. & Pfaff, D. W. The hypothalamic ventral premammillary nucleus: A key site in leptin's regulation of reproduction. *J. Chem. Neuroanat.* **61-62**, 239–247 (2014).
37. Soden, M. E. *et al.* Genetic isolation of hypothalamic neurons that regulate context-specific male social behavior. *Cell Rep.* **16**, 304–313 (2016).
38. Stagkourakis, S. *et al.* A neural network for intermale aggression to establish social hierarchy. *Nat. Neurosci.* **21**, 834–842 (2018).
39. Chen, A.-X. *et al.* Specific hypothalamic neurons required for sensing conspecific male cues relevant to inter-male aggression. *Neuron* **108**, 763–774.e6 (2020).
40. Ross, R. A. *et al.* PACAP neurons in the ventral premammillary nucleus regulate reproductive function in the female mouse. *Elife* **7**, e35960 (2018).
41. Gegenhuber, B. & Tollkuhn, J. Signatures of sex: Sex differences in gene expression in the vertebrate brain. *Wiley Interdiscip. Rev. Dev. Biol.* **9**, e348 (2020).
42. Dodero, L. *et al.* Neuroimaging evidence of major morpho-anatomical and functional abnormalities in the BTBR T+TF/J mouse model of autism. *PLoS One* **8**, e76655 (2013).
43. Wu, C. *et al.* RollFISH achieves robust quantification of single-molecule RNA biomarkers in paraffin-embedded tumor tissue samples. *Commun Biol* **1**, 209 (2018).
44. Xia, C., Babcock, H. P., Moffitt, J. R. & Zhuang, X. Multiplexed detection of RNA using MERFISH and branched DNA amplification. *Sci. Rep.* **9**, 7721 (2019).
45. Choi, H. M. T. *et al.* Third-generation in situ hybridization chain reaction: multiplexed, quantitative, sensitive, versatile, robust. *Development* **145**, (2018).

Methods:

Encoding Matrix Design

Encoding Matrix was fit using SMART-seq data collected from the mouse whole cortex and hippocampus due to its high capture efficiency per cell [1]. Gene expression was normalized to a total sum of 100,000 Genes with an average expression below 1 in any cell type were removed to encourage weight assignment to higher expressed genes. Genes that had an average expression above 100 in any cell type were also removed to encourage the use of more genes as highly expressed genes have a strong effect on reconstruction accuracy as well as cell type distances purely due to magnitude. Potential encoding probes were designed for each gene using Paintshop with a probe length of 30bp. Genes were further filtered if no probes could be designed. Reference dataset was class balanced to the cluster level to ensure that rarer cell types had a meaningful effect on the design. Encoding matrix was fit using a modified version of Discriminant Projective Non Negative Matrix Factorization (DPNMF [2,3]) which consists of a discriminant aspect that maximizes the variance between cell types while minimizing the variance within a cell type as well as a reconstructive aspect that increasing the accuracy of gene reconstruction. A high mu value of 50 was used for the discriminant aspect ensuring that more weight was applied to the discriminant aspect than the reconstruction aspect. The resulting loading matrix was scaled bitwise and integerized to maximize the utilization of the encoding probes that were designed for each gene. This involved clipping the highest weighted genes per bit and scaling so that the highest weighted genes utilized all encoding probes that were possible for those genes. The integerized encoding matrix was then clipped for each gene at the maximum number of probes that could be designed for that gene (i.e. if a gene only had 27 probes but needed a weight of 30 the encoding matrix was clipped to 27). Resulting encoding matrix consisted of 6,654 Genes and 35,919 Probes.

Encoding Probe Design

A complex oligo pool of encoding probes was designed for ATLAS consisting of 35,919 encoding probes, targeting 6,654 genes. ATLAS encoding probes were engineered to contain a 30-nucleotide target sequence with specific homology to the mRNA of interest. The targeted sequences for the encoding probes were designed to have a GC content ranging from 45% to 65%, resulting in a melting temperature between 65°C and 72°C. 20-nucleotide readout arms were appended to the ends of the target sequence, and concatenated by two flanking regions designed for primer amplification. Two primers, a forward and reverse, were designed for the initial amplification of the oligo pool, with minimal homology, to any encoding probe. The reverse primer was designed with a NheI restriction digest site, used in later steps. An additional forward primer containing a T7 promoter was also designed for subsequent rounds of PCR amplification.

For marker gene validation probes, an oligo pool of 16,320 encoding probes was designed to target 170 genes. The probe design follows the same structure as the ATLAS probes, with the key difference being that four readout arms were appended to the ends of the target sequences instead of three. Additionally, the same forward and reverse primers were incorporated at the ends of the probes.

Encoding Probe Amplification

The template molecules for the ATLAS oligo pool (Twist Biosciences) were amplified in two limited cycle PCR reactions to minimize the formation of nonspecific products. A small-scale PCR reaction was first carried out using 0.4 ng/uL of the initial Twist template, following the manufacturer's recommended guidelines. KAPA HiFi hot start ready mix (Fisher Scientific, 50-196-5217) was used for PCR amplification, with 0.3 µM of primers. The initial template amplification did not include the forward primer with T7 promoter. The correct product size was validated on an Agilent 2100 bioanalyzer and then on a 15%TBE-Urea polyacrylamide gel (Thermo Fisher Scientific, EC68852BOX) in every step after that. The PCR product was cleaned using a phenol-chloroform extraction and desalted using a 10 kDa centrifugal filter column (Sigma Aldrich, UFC5010). The amplified product was used as the template for the second PCR reaction at 0.04 ng/uL per reaction volume. Product was amplified with KAPA HiFi hot start ready mix and 0.3 µM T7 forward primer, adjusting the melting temperature accordingly. For marker gene validation probes, the second PCR reaction was performed with 0.3 µM T7 reverse primer. Elongation times for the second reaction were also increased to 45 sec, deviating from Twist recommendations of 15 seconds. To enhance probe penetration, the PCR product was digested overnight at 37°C with 1 unit of NheI-HF (New England Biolabs, R3131) per µg of product, reducing the size of the encoding probes from 113 nt to 94 nt.

Digested PCR products were converted to RNA encoding probes using a high yield in vitro transcription (IVT)

kit (New England Biolab, E2040S). Reaction concentrations were maintained as per the manufacturer's recommendations, with the exception of CTPs (Thermo Fisher Scientific, R0451), which were added to the reaction volume at a final concentration of 5 mM. IVT amplification was carried out overnight at 37°C before cleaning and desalting as described above. The final concentration of encoding probes was quantified using a BR RNA Qubit kit (Thermo Fisher Scientific, Q10210) and size verified via gel electrophoresis. RNA encoding probes were aliquoted into 1.5 mL tubes, with 600 µg allocated per experiment. The encoding probes were dried completely using a speedvac and stored at -80°C until further use. The same protocol was followed for the preparation of nonspecific encoding probes.

For marker gene validation probes, IVT products were converted to DNA encoding probes using Reverse Transcriptase (Maxima H Minus Reverse Transcriptase, EP0751). Reaction concentrations were maintained as per the manufacturer's recommendation with 40 µM forward primer containing a Uracil at the 3' end. RT was carried out overnight at 53ºC before cleaning and desalting as described above. To enhance probe penetration, the RT product was digested overnight at 37°C with 1 unit of USER Enzyme (New England Biolabs, M5505L) per µg of product, reducing the size of the encoding probes from 150 nt to 130 nt. DNA encoding probes were aliquoted into 1.5 mL tubes, with 100 µg allocated per experiment. The encoding probes were dried completely using a speedvac and stored at -80°C until further use.

Coverslip Functionalization

Coverslips (40 mm, #1.5; Bioptechs, 40-1313-03193) were cleaned by submerging in a 1:1 solution of 37% HCl and methanol with sonication for 30 minutes. They were then rinsed twice with deionized water and once with 100% ethanol, each for 5 minutes, before being dried completely at 70°C. The coverslips were subsequently submerged in a mixture of 0.1% (v/v) triethylamine (Sigma Aldrich, 471283) and 0.2% (v/v) allyltrichlorosilane in chloroform for 30 minutes. After rinsing once in chloroform and twice in 100% ethanol, the coverslips were dried at 70°C. They were then treated with 2% (v/v) (3-Aminopropyl)triethoxysilane (APES, Sigma Aldrich, 440140) in acetone for 10 minutes, followed by two 5 minute rinses in deionized water and once in 100% ethanol. The coverslips were dried once more at 70°C and stored under vacuum until further use. Functionalization treatment is necessary for improved tissue and gel adhesion to coverslips [4].

Animals

Adult BTBR *T+ Itpr3tf*/J male and C57Bl6/J male and female mice aged 56 days were used for this study. To reduce the stress of animals due to shipping and handling, mice were maintained for one week upon arrival on a 12 hour:12 hour light/dark cycle with access to food and water before sectioning.

Sectioning

Whole mouse brains were harvested at 8 weeks of age and perfused promptly in 1x PBS (Thermo Fisher Scientific, 10010049) with 0.1% (v/v) Tween-20 (Sigma Aldrich, P1379) and 3 mg/mL Poly(vinylsulfonic acid, sodium salt) solution (PVSA, Sigma Aldrich, 278424) (1x PBSTw). Samples were embedded in optimal cutting temperature (OCT, Fisher Scientific, 23-730-571) compound immediately and flash frozen in liquid nitrogen before being stored at -80°C. The day before sectioning, samples were mounted onto a cryostat specimen disk and stored at -20°C allowing the sample to equilibrate to sectioning temperatures. A cryostat was used for serial sectioning of the central brain region (CCFx 4.5-9.5mm) for each animal. Each series consisted of 24-20 µM thick coronal sections with an even spacing of 200 µM between sections. Sections were distributed 4 per coverslip and fixed soon after. Three technical replicates were obtained for each series generated.

Fixation

Before fixation, samples were allowed to sit for 5 minutes to ensure proper tissue adhesion to the coverslip. The sections were then fixed with 4% (v/v) paraformaldehyde (PFA, Electron Microscopy Sciences, 15714) in 1x PBScontaining 3 mg/mL PVSA for 10 minutes , followed by three 5 minute washes in 1x PBSTw. Sections were stored in 70% ethanol at -20°C until further use.

Permeabilization

Samples were stored for a minimum of 72 hours to a maximum of 4 months before preparation. Upon removal from storage conditions, samples were washed three times in 1x PBStw for 5 minutes at room temperature, and permeabilized in 1x PBS containing 1% (v/v) Triton X-100 (Sigma Aldrich, X100) and 3 mg/mL PVSA for 30 minutes at 47°C with constant agitation.

MelphaX RNA modification

Following permeabilization, the samples were rinsed three times in 20 mM MOPS (pH 8) containing 0.1% (v/v) Tween-20 and 3 mg/mL PVSA at 47°C for 5 minutes each. After the final rinse, the samples were aspirated dry, and 100 µL of 0.5 mg/mL MelphaX diluted in MOPS buffer was pipetted directly onto tissue sections for RNA modification. To prevent evaporation, a small piece of parafilm was placed over the MelphaX solution, and the samples were incubated at 47°C for 1 hour. MelphaX was prepared according to EASI-FISH protocol [5].

Hydrogel embedding

After RNA modification, samples were rinsed three times for 5 minutes in 1xTBS (2 mM TRIS 300 mM NaCl) with 0.1% (v/v) Tween-20 and 3 mg/mL PVSA (1xTBStw) at room temperature. A gel solution containing 3% 19:1 acrylamide:bis-acrylamide (Sigma Aldrich, A3449) in 1xTBS with 0.1% (v/v) Tween-20 and 3 mg/mL PVSA was prepared for sample hydrogel embedding. 3 mLs of gel solution were made per coverslip and split, with 2mLs containing 0.1% (v/v) N,N,N′,N′-Tetramethyl ethylenediamine (TEMED, Sigma Aldrich, T7024) and 1 mL containing 1% (w/v) Ammonium persulfate (APS, Sigma Aldrich, A3678). Gel solution containing TEMED was added to samples for 30 minutes under vacuum allowing the solution to penetrate into the tissue sections. After degassing, the 1 mL of gel solution containing APS was added to the sample and briefly mixed by pipetting. A pedestal containing a coverslip, treated with gel slick (Lonza, 50640) was inverted onto the sample to form a gel between the pedestal and the sample, the excess gel solution was aspirated off. Samples sat for 2 hrs allowing the gels to polymerize fully before being separated from the pedestal with a razor blade.

Pre-Clearing

Samples were washed three times for 5 minutes with 1xTBStw at 47°C. A 2% (v/v) sodium dodecyl sulfate (SDS, Thermo Fisher Scientific, AM9820) solution in 1xTBS with 0.1% Tween-20, 3 mg/mL PVSA, and 1% (v/v) proteinase K (New England Biolabs, P8107S) was used to clear the sample. Digestion was carried out at 47°C with agitation for 18 hrs and then rinsed three times for 5 minutes with 1xTBStw. All steps in clearing, including the washes before and after, should be done at 47°C to avoid precipitation of SDS.

Encoding

A 50% (v/v) formamide (Thermo Fisher Scientific, AM9344) solution in 1xTBS with 0.1% Tween-20 and 3 mg/mL PVSA was used to equilibrate the sample in a hybridization buffer for 10 minutes at 47°C. Each coverslip was aspirated dry and hybridized with 30uL of encoding solution containing 600 ug of RNA encoding probes (150 ug/section) in 50% (v/v) formamide with 10% (w/v) dextran sulfate (Sigma Aldrich, D6924) and 1xTBS and 0.1% Tween-20 and 3g/mL PVSA. The encoding solution was pipetted directly onto the sample before being covered with a parafilm square. Hybridization of encoding probes was carried out for 18 hrs before being washed 4 times for 15 minutes at 47°C with agitation in 50% formamide in 1xTBS with 0.1% Tween-20 and 3 mg/mL PVSA . For MERFISH, encoding was done with 30% (v/v) formamide at 37ºC since the probes are DNA.

Post-Clearing and Hydrogel embedding

Samples were washed three times with 1xTBStw for 5 minutes at 47°C and cleared a second time to further reduce encoding probes that may have bound non-specifically. Clearing was done for 3 hrs, as described above, and then washed with 1xTBStw at 47°C. A second hydrogel was formed on the sample, as described above, to reduce any lifting caused by tissue clearing of dense brain regions. Sample was washed three times in 1xTBStw for 5 minutes and stored in a 10% formamide solution in 1xTBS with 0.1% Tween-20 and 3 mg/mL PVSA at 4°C

Automated Data Collection Hardware & Software

We developed a custom fluidics system to enable continuous high-throughput imaging across six 40-mm coverslips, addressing limitations of commercial fluidics systems in multiwell, high-flow environments. Our system allows for simultaneous imaging and hybridization by alternating between two groups of wells, significantly reducing liquid handling time and maximizing throughput.

A chamber was designed with six 35 mm wells, creating a watertight seal with the coverslips while preserving imaging space. The wells were configured in a tight two-by-three arrangement, fitting in the stage adapter footprint, with four M3 screw holes surrounding each well. This profile was used to mill 2 mm stainless steel plates for compressing the chamber and providing a flat imaging plane. The edges of the chamber design were then inset by 0.5 cm to account for expansion once assembled. To create the chambers, a negative mold was designed and 3D printed using PETG. Two part silicone was mixed and degassed for 15 minutes to minimize large bubbles in the chamber. The silicone was then poured into the mold and allowed to set overnight at room temperature.

The chamber is assembled by aligning a steel plate with a silicone chamber placed on top of it. Coverslips are

then placed on top of the silicone chamber with samples facing the steel plate. A second steel plate is then placed on top of the samples and secured to the chamber using four M3x16 coverslips around each sample. The bottom of each sample is then cleaned using lens cleaner and lens paper, and a small sticker was added to the edge of each coverslip to serve as a reference point for autofocus. Once placed on the microscope, fluidics is integrated using a 3D printed lid, holding blunt-tipped needles in each chamber at an angle to prevent vacuum formation. This open-well design supports milliliters-per-second flow rates, substantially improving throughput compared to traditional closed chambers.

To accomplish milliliters-per-second flow rates a fluidics system was assembled consisting of a syringe pump, multiposition valves and python software control allowing automated control of up to 30 readout hybes as well as strips on 6 large sample wells. A 5mL glass syringe was used to minimize system maintenance and improve system reliability at high flow rates. Vici 10-24 port multiposition valves were daisy chained to enable easy expansion to large numbers of readout solutions. Fluidics tubing ranged from 1/16 inch in paths that were shared across multiple solutions and 1/8 inch diameter for tubing that goes directly to solutions allowing for faster flow rates. Additional features including vacuum aspiration for faster liquid removal and syringe mixing within open wells were added to improve reproducibility.

Custom python software (GITHUB LINK) integrates the fluidics system with ATLAS protocols, featuring a modular, file-based control system compatible with microscope software control. The user-friendly GUI allows for real-time simulation of protocols and manual control, facilitating flexible protocol development and execution.

Chamber preparation for data acquisition

Fluidics system was cleaned by flushing with ethanol and rinsed with 1xTBStw before each experiment and stored in Ethanol for longer durations. Deep cleaning was performed by flushing with 10% Bleach before standard cleaning if contamination was suspected. Up to 6 coverslips were assembled into each chamber. Samples were stained with 1xTBS with 0.1% (v/v) Tween-20 and 3 mg/mL PVSA with 2ug/mL 4’,6-diamidino-2-phenylindole (DAPI, Sigma Aldrich, D9542) for 5-10 minutes at room temperature manually and rinsed three times with 1xTBS with 0.1% (v/v) Tween-20 and 3 mg/mL PVSA before being attached to the fluidics system.

Data Collection

Images were captured on a custom Epifluorescent microscope with a 10X/0.45 NA Objective. Excitation light was provided by Solis LEDS for imaging Cy5 disulfide conjugated readout probes and PCB mounted LEDs for imaging dapi for nuclear stain. Emission was collected on FLIR Blackfly USB Camera with a pixel size of 0.425-0.49 µm. Microscope was controlled via Micromanager and custom MATLAB interface [6].

Focus and Position Selection

Initial focus was set manually and entire coverslips were imaged to visualize dapi. Positions containing sections were manually selected using a custom drawing script. 5 evenly spaced positions were manually focused for each section as well as a reference position containing a registration sticker per coverslip. A plane was fit for these positions per section to extrapolate focus and set relative to the registration sticker focus. Before each round of imaging the registration sticker was imaged and the focus plane was adjusted to ensure cells were in focus across the multiple days of staining, striping and imaging.

Automated Strip

Samples were stripped from fluorophores similar to MERFISH protocol [4] and imaged before the hybridization of each new readout probe, allowing them to be used as a background image for downstream analysis. Fluorophores attached with a disulfide to readout probes were stripped from the sample with 2.5 mL of 0.25 mM Tris(2-carboxyethyl)phosphine hydrochloride (TCEP, AKSci, X4741) in 1xTBS with 0.1% (v/v) Tween-20 and 3 mg/mL PVSA . Samples were incubated in TCEP solution at room temperature for 30 minutes, and mixed once halfway through before being rinsed three times with 1xTBStw before imaging.

Automated Hybridization

Samples were briefly rinsed once in 30% (v/v) formamide in 1xTBS with 0.1% (v/v) Tween-20 and 3 mg/mL PVSA with 2ug/mL 4’,6-diamidino-2-phenylindole (DAPI, Sigma Aldrich, D9542). Readout probes, diluted to 10 nM in 30% (v/v) formamide in 1xTBS with 0.1% (v/v) Tween-20 and 3 mg/mL PVSA and 2ug/mL DAPI, were added to the sample. Hybridization of readout probes was carried out for 30 minutes at room temperature, with one mixing step half way through. Excess readout probes not bound were washed from the tissue three times with 30% (v/v) formamide in 1xTBStw with 2ug/mL DAPI, and twice with 1xTBStw, before imaging.

Image Processing

Raw images were processed using custom python code available in the project's Github repo. In short, raw images were binned to a pixel size of 0.85-0.98 μm. Camera constant and excitation light contamination was experimentally calculated for each acquisition and subtracted. Uneven illumination and emission capture was experimentally calculated for each acquisition and corrected. Images were subjected to a 2 pixel median low pass filter to remove hot or dead pixels as well as a 25 pixel sigma rolling ball high pass filter to remove residual constant as well as background that is much larger than cells.

Background acquisitions were registered to readout acquisition using cross correlation on dapi images. Background acquisitions were then subtracted from readout acquisitions for only the signal channel. Processed images were then registered to a reference hybe and stitched together using cross correlation of dapi images.

Cells were segmented using Cellpose [7] cyto3 model on the stitched reference dapi image for nuclei as well as a max projection of all readout images for total cell. Missed cells in dense areas were recovered by calling peaks in dapi images and morphologically dilating to a 5 μm radius. For each cell the median of the segmented pixels for each measurement was calculated and saved for future analysis as well as the cells segmentation properties and spatial coordinates.

Common Coordinate Framework Registration

Each section was registered to the common coordinate framework by first assigning an approximate ccf x through visual inspection with reference MERFISH data. Registration in z and y were performed by manually clicking registration points and fitting a radial basis function model to convert from experimental spatial coordinates to CCF coordinates.

Low Quality Cell Filtering

Non cells were removed as cells below a sum signal threshold as well as beyond 50um from a connected component graph created from the spatial coordinates of all cells. Low Quality cells due to hydrogel integrity or registration errors were removed as any cell that had a dapi signal decrease of more than 50% in 2 or more rounds.

Cell Scalar Correction

To correct for uneven staining and total RNA content the overall magnitude of each cell vector was normalized. First a robust magnitude was approximated by correcting bits where cells were outliers and then taking the sum of the corrected cell vector. Cells were normalized by scaling their approximate magnitudes to the same value. Residual scalar differences due to the position of each cell in the optical field of view were corrected by fitting a linear regression between image coordinates and each measurement.

Unsupervised Clustering

Measured cell vectors were normalized bitwise by centering around the median and scaling by the robust standard deviation of the 1st to 99th percentile cells for each bit. An igraph implementation of leiden was then performed with a high resolution parameter. Clusters within correlation of 0.9 were then merged.

Decoding & Harmonization.

To decode ATLAS signatures into predefined cell types, we employed a Bayesian recursive harmonization and classification approach called SCALE (Single Cell Alignment Leveraging Existing data). This method maximizes the use of reference atlas data and incorporates spatial priors derived from the anatomical structure of the brain.

Reference ATLAS Vectors: Reference ATLAS vectors were computed by projecting scRNAseq data through the DPNMF projection matrix, reducing the data to an 18-dimensional space. This dimensionality reduction enabled us to align the scRNAseq data with spatial transcriptomic signatures measured by ATLAS.

Spatial Priors: Spatial priors for each cell were generated using a kernel density estimate of cell type distributions based on CCF-registered reference MERFISH data. The kernel density was approximated by using numpy histogramdd on the ccf coordinates for each type with a binsize of 100 μm. The three dimensional histogram was then smoothed using a gaussian filter with a sigma of 100 μm in the CCF y and z axes and 250 μm in the x-axis. To calculate the spatial prior of a single cell, the ccf coordinates of that cell were used to pull the density estimate of each cell type in that location, normalizing to a sum of 1. These spatial priors represent the probability of finding

specific cell types in certain brain regions, leveraging known anatomical structures. Spatial probability maps for each subclass were constructed across the brain using these priors.

Balanced Reference Vectors: To ensure an even comparison across sections, reference vectors were sampled based on the average spatial priors of all cells in a given section, creating a section-balanced reference. Reference vectors and measured vectors were normalized using robust magnitude and bitwise corrections.

Initial Neuron vs Non-Neuron Classification: Unsupervised clusters using cellular transcriptional signatures were classified into neurons and non-neurons using a pynndescent based KNN classifier trained on section-balanced reference cells with euclidean as the metric and 25 neighbors. After this neuron/non-neuron classification, the spatial priors were updated to include either only neurons or only non-neurons, depending on the classification of the cluster.

Recursive Subclass Classification: For subclass-level classification, we employed a recursive decision tree method. The decision tree structure was constructed by averaging the cell type vectors from reference scRNA-seq data and fitting a dendrogram based on pairwise correlations. At each binary decision point in the tree, two operations were performed:

1. Posterior Probability Calculation: For each cell, the posterior probability of belonging to one of the two subtrees was calculated. This was done by combining the spatial prior with the likelihood of the cell type, inferred from a sklearn logistic regression classifiers trained on section-balanced reference cells.
2. Harmonization: After each binary decision, the median and robust standard deviation (std) of the measured data were aligned with reference cells within the selected subtree. This linear correction ensured that the measured data was harmonized with the reference scRNAseq data.

Final Subclass Assignment and Imputation: Cells continued through this recursive decision process, moving down the decision tree and being harmonized at each step until they reached a final subclass label at the leaves of the tree. At this point, cell types were assigned, and the data was fully harmonized with the reference atlas. Imputation of transcriptomes was then performed using a nearest neighbors approach based on transcriptional signatures. Using the harmonized vectors for the measured cells the 15 nearest reference neighbors were calculated using pynndescent based KNN with euclidean as the metric. Imputed expression was calculated as the average gene expression for these 15 reference cells.

Validation - pairing two datasets.

The accuracy of imputation was calculated using pseudo-pairing procedure. Two matching sections from different datasets (e.g.. ATLAS imputed and MERSCOPE) based on CCFx values after registration done as described above. To account for overall sampling frequency the total number of cells were downsampled to the same number. Cells were then paired across datasets in a greedy pairing algorithm, as finding global optimal pairing was too computational time consuming. The greedy pairing first created a list of all candidate pairing of all pairs of cells 100 um from each othe. The correlation score for all candidate pairs was calculated based on the Pearson correlation of the log gene expression across the 336 shared genes among all brain atlases. The correlation scores were sorted from highest to lowest, and the greedy algorithm selected pairing according to this sorted list after each selection, excluding possible pairing that included a cell that was just paired. The output of this pairing algorithm was the correlation score between all optimally paired cells. The cumulative distribution function of these correlation scores was used to evaluate the quality of agreement between the two datasets. Higher agreement results in increased area under the curve and more cells above each threshold.

Validation marker gene selection

The genes for MERFISH validation of subclass types were selected from a set of 500 genes in the referenced MERFISH data. Genes that contributed most to subclass classification were prioritized by selecting those with the highest F1 scores. To enhance the signal in MERFISH imaging, genes with more than 96 hybridization probes were chosen. The number of bits also aligned with the number of hybridization rounds used in the ATLAS data collection, while maintaining a Hamming-Distance-4 for error correction. 17 ‘blank’ barcodes were included to measure the false-positive rate in MERFISH measurement, resulting in a final selection of 170 genes.

Validation marker gene MERFISH Imaging

Images were captured on a custom Epifluorescent microscope with a 63x Objective. The excitation light for imaging Cy5 was consistent with the ATLAS protocol. The PCB-mounted UV LED was used for imaging the fiduciary markers and dapi. Emission was collected with a pixel size of 0.083 μm. For each position, 4 z-indexes were

captured per dataset with 1 μm spacing. MERFISH imaging was done using FCS2 chambers as described [4].

Validation marker gene - combining ATLAS and MERFISH analysis

After completing the 18 rounds of MERFISH hybridization and imaging, the FCS2 chamber was disassembled, and the coverslip with the tissue was placed in a petri dish. To remove the marker gene DNA encoding probes, the sample was washed 4 times for 15 minutes at 47°C with agitation in 50% formamide in 1xTBS with 0.1% Tween-20 and 3 mg/mL PVSA. The sample was hybridized with the ATLAS encoding probes following the previously described protocol. The fluidics system was cleaned as outlined earlier, and the microscope objective was switched to 10x. After the post-encoding clearing and washes, the sample was assembled back into the FCS2 chamber and imaged according to the ATLAS protocol.

Validation marker gene MERFISH Image Analysis

Image analysis was performed using custom Python code (GITHUB LINK). In short images were corrected by replacing hot pixels with the medians of their immediate neighbors before being subjected to a highpass and lowpass filter to remove background and high frequency noise. Readout rounds were registered to a reference hybe using fiduciary markers. Spots were called with trackpy locate (link). Spots were paired across rounds of hybridization into candidate transcripts. Transcripts that matched designed barcodes within 1 error were assigned to cells using a segmentation mask generated with cellulose (link) on dapi images. Cells with fewer than 10 transcripts were removed. Individual fields of view were registered between MERFISH segmentation and ATLAS segmentation using a rigid transformation to minimize the residual distance between paired segmentation masks. Cells with paired masks that were larger than 2 um were filtered to ensure accurate pairing between datasets.

Construction of 3D volumetric cell type inference

To analyze the spatial distribution of cell types across mouse brain samples, we developed a data processing pipeline to convert individual cell coordinates and types into a standardized 5D tensor. For each of the 15 animals, the X, Y, Z coordinates and cell types were binned into a 100 μm grid in the tissue section plane (CCF z and CCF y) and 300 μm along the anterior-posterior (AP) axis, which accounts for the 200 μm sectioning performed. The AP axis was upsampled by a factor of 3 relative to the tissue section plane to increase resolution and create an isotropic matrix. This binning was implemented for each animal and cell type using NumPy's `histogramdd` function.

A key challenge was managing incomplete data due to section tears and holes. Voxels with cell counts below 50% of the average cell count per voxel were replaced with NaN values. To address unequal sampling densities across animals, a correction factor was applied based on the average number of cells per voxel across all samples, assuming that total cell counts per voxel remain constant across animals. A Gaussian filter with sigma of 150 μm was applied to the data with to reduce noise and interpolate values in low-density regions. The resulting 4D tensors from each animal were then stacked to create a 5D tensor (sample, X, Y, Z, cell type).

Comparative analysis - cell type spatial distributions.

The statistical analysis of cell type distributions used the 5D tensors described above. Assuming brain symmetry, the tensors were reshaped so that the two hemispheres from each section were treated as separate samples, with one hemisphere flipped horizontally. For each comparison (male vs. female or B6 vs. BTBR), the relevant hemispheres were selected. For each cell type, the average counts at each voxel were calculated and rescaled to have the same mean, ensuring that the identified differences reflected spatial changes rather than global abundance.

A per-voxel 3D matrix of the differences between the two distributions was then computed. The residuals from this comparison were used to calculate the entropy of the spatial distributions. Residuals made the comparison spatially explicit, as voxel-wise abundance was compared across identical locations. Entropy was chosen to quantify the overall extent of the differences, with identical distributions yielding zero residuals and thus zero entropy, and highly distinct distributions producing high entropy.

To assess statistical significance, we applied a permutation procedure, where sample indices were permuted before averaging for each cell type. This allowed estimation of the probability distribution for the residual entropy. We used an adaptive sampling approach, performing an initial 1,000 permutations for each cell type and extending to 10,000 permutations when p-values were estimated to be smaller than 0.005.

Comparative analysis - regional compositional analysis.

Similar to the cell type analysis, the regional analysis used the inferred 5D tensors as input, assumed brain symmetry, and calculated the average 4D tensor (X, Y, Z, Type) for each condition (B6 male, B6 female, BTBR male). For each voxel, the correlation distance (1 - Pearson correlation coefficient) between the type distributions of the two conditions was calculated. This correlation distance was then compared to a null distribution generated through a permutation procedure, as described in the cell type analysis. We used a similar adaptive procedure for p-value estimation, starting with 1,000 permutations and extending to 10,000 when p-values were smaller than 0.005.

Additional References

1. Yao, Z. *et al.* A taxonomy of transcriptomic cell types across the isocortex and hippocampal formation. *Cell* **184**, 3222–3241.e26 (2021).
2. Guan, N., Zhang, X., Luo, Z., Tao, D. & Yang, X. Discriminant projective non-negative matrix factorization. *PLoS One* **8**, e83291 (2013).
3. Song, D., Li, K., Hemminger, Z., Wollman, R. & Li, J. J. scPNMF: sparse gene encoding of single cells to facilitate gene selection for targeted gene profiling. *Bioinformatics* **37**, i358–i366 (2021).
4. Moffitt, J. R. & Zhuang, X. Chapter One - RNA Imaging with Multiplexed Error-Robust Fluorescence In Situ Hybridization (MERFISH). in *Methods in Enzymology* (eds. Filonov, G. S. & Jaffrey, S. R.) vol. 572 1–49 (Academic Press, 2016).
5. Wang, Y. *et al.* EASI-FISH for thick tissue defines lateral hypothalamus spatio-molecular organization. *Cell* **184**, 6361–6377.e24 (2021).
6. Edelstein, A. D. *et al.* Advanced methods of microscope control using μManager software. *J Biol Methods* **1**, (2014).
7. Stringer, C., Wang, T., Michaelos, M. & Pachitariu, M. Cellpose: a generalist algorithm for cellular segmentation. *Nat. Methods* **18**, 100–106 (2021).

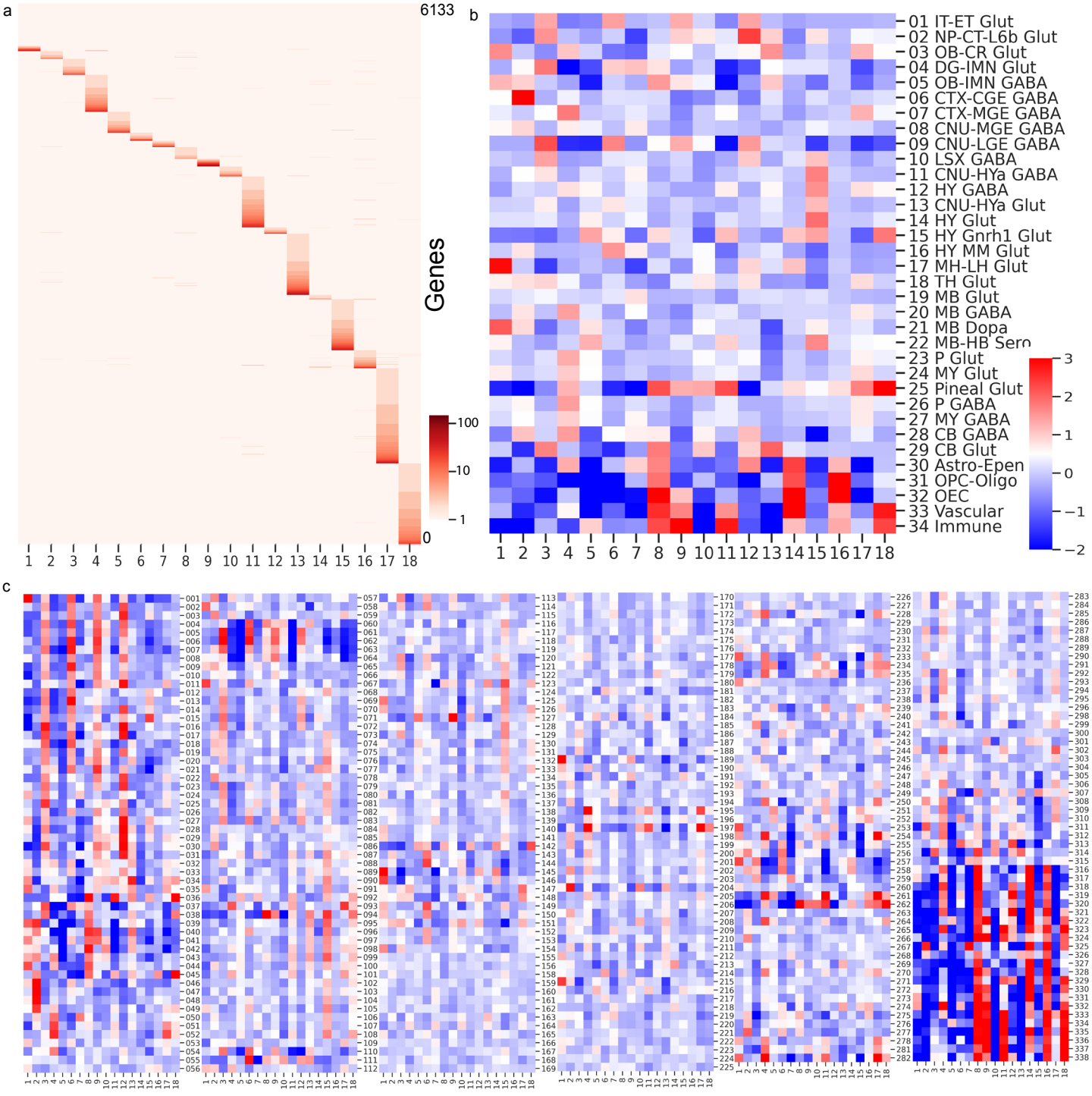

Extended Figure 1:ATLAS DPNMF Encoding Design. (a) Heatmap of the DPNMF Encoding Matrix showing the Log Weight of each gene on each measurement. weights directly translate into the number of encoding probes per gene per measurement. (b) Heatmap of the expected cell vector for each class level cell type calculated by projecting scRNAseq using DPNMF encoding matrix and averaging across cell types. zscore normalized. (c) 336 subclass level expected cell type vectors. zscore normalized

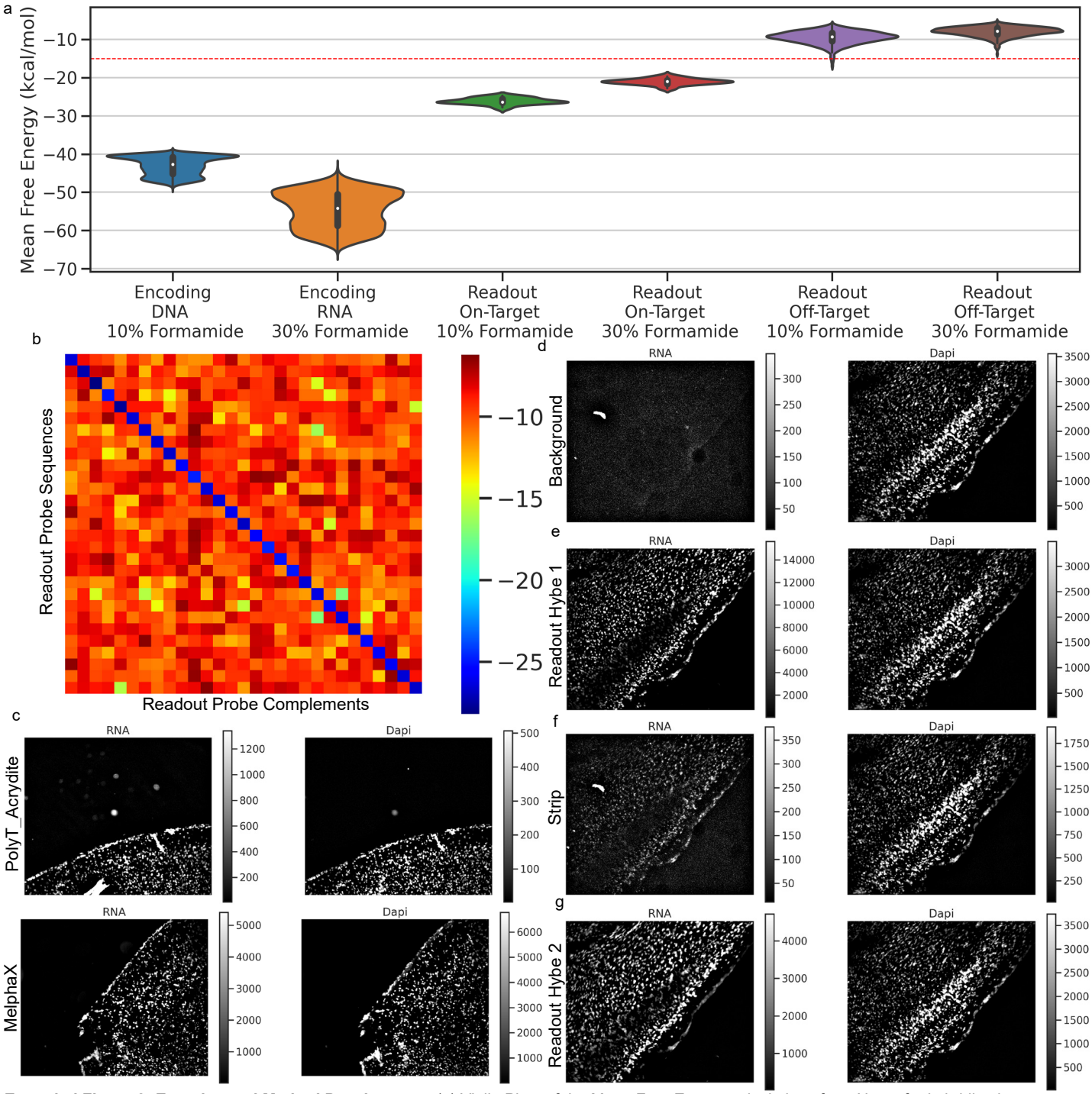

Extended Figure 2: Experimental Method Development. (a) Violin Plots of the Mean Free Energy calculations from Nupacfor hybridization event structures. (b) pairwise heatmap of On and Off Target structure MFE stability scores. (c) Comparison of the RNA and DNA signal between hydrogel anchoring strategies (PolyT_Acrydite a hybridization based approach and MelphaX a covalent approach). (d) Visual of the low background present in the RNA channel prior to Readout hybridization. (e) Example of signal observed with ATLAS signatures. (f) Residual signal remaining after TCEP reduction of disulfide readout probe. (g) Subsequent Readout hybe which contains signal from Readout hybe 2 as well as residual signal from Readout Hybe 1.

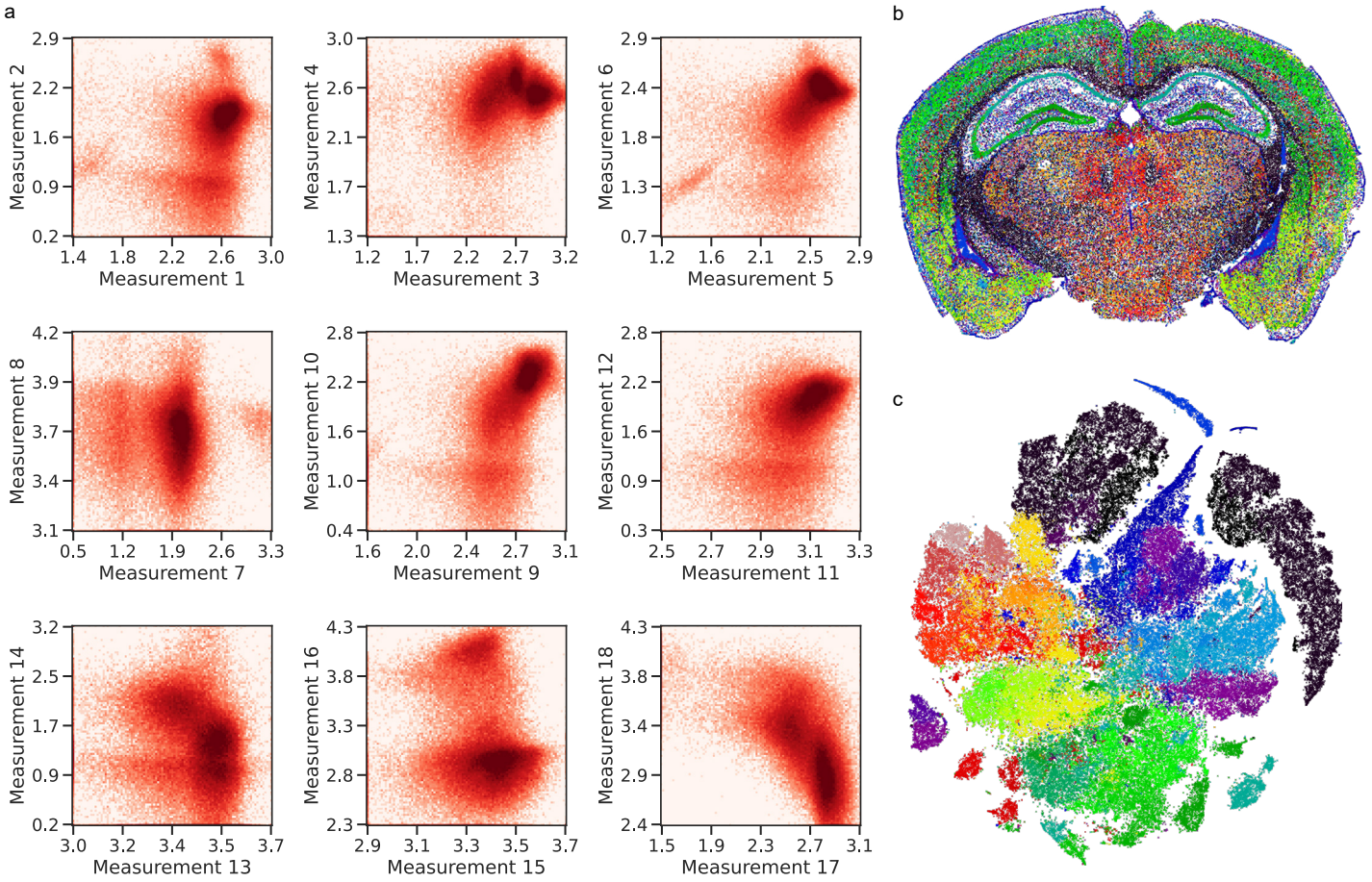

Extended Figure 3: ATLAS Transcriptional Signature measurements. (a) Visualization of the content of all 18 Measurements for a single section. Multiple modes of density can be seen within each pairwise log 10 scale signal plot. (b) Unsupervised clustering of measured cells for a single section. Spatial locations of each cluster of cells (c) TSNE locations of each cluster of cells

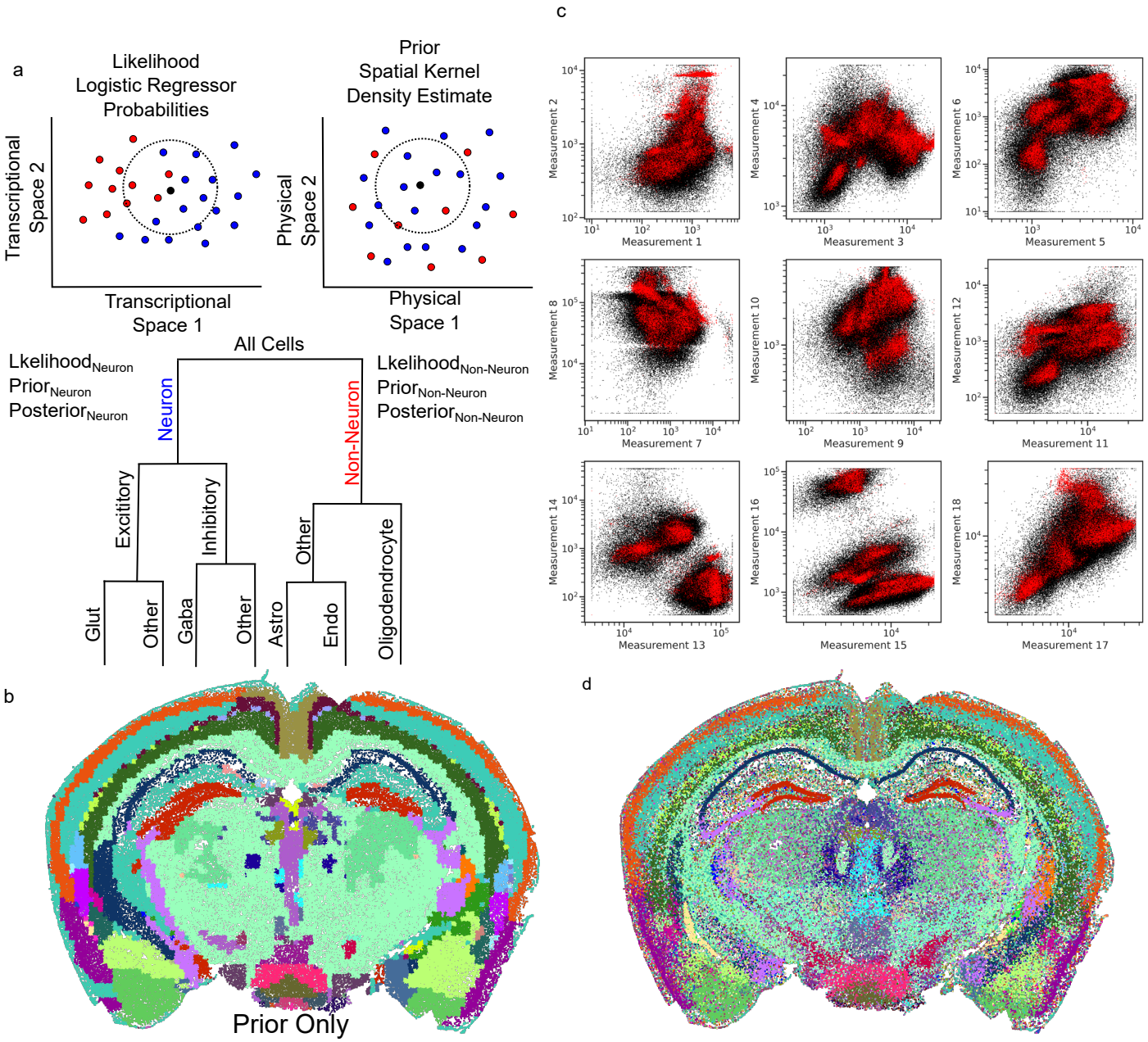

Extended Figure 4: Decoding and Harmonizing. (a) Cartoon diagram showing decoding strategy. individual cells walk down a decision tree of cell types. Decisions are made by taking the likelihood that a cell is a cell type based only on features calculated using a logistic regressor trained on reference scRNAseq cells and the Spatial prior expectation of what cell types are present in that cells physical location calculated using a kernel density estimate with a ccf)z and ccf_y sigma of 100 um and ccf_x of 250 um on referenece MERFISH data. (b) Visual Representation of the Spatial Prior demonstrated by passing measured cells through the decoder ignoring likelihood. (c) Results of Data Harmonization. Cells are shown for each measurment colored by source. Black for reference scRNAseq and Red for harmonized measured ATLAS cells. (d) Results of Data Decoding at the subclass level.

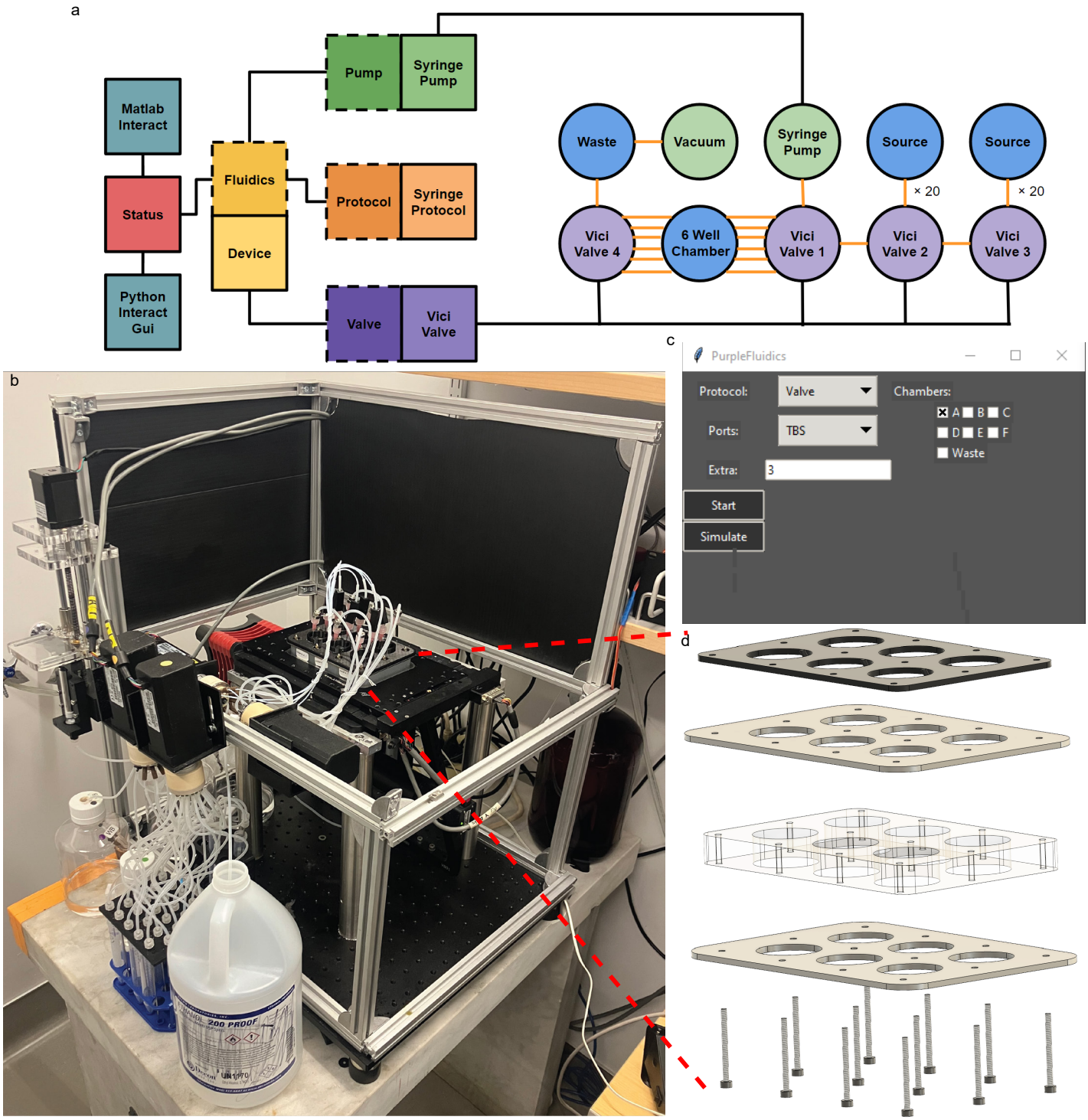

Extended figure 5: Automated Open Chamber Fluidics System. (a) Schematic Design of Fluidiics software (squares) and hardware (circles). Liquid is extracted from source tubes using automated syringe pump and valves and deposited on sample coverslips. Waste is removed in reverse. Object oriented software implementation allows for modular integration of multiple device drivers as well as multiple units of each device. Current implementation allows for up to 30 rounds of readout hybridization and 30 rounds of stripping across each of 6 experimental wells. (b) Picture of Custom epifluorescent microscope with open source fluidics system attached. (c) visual of Graphical User Interface which allows manual control when software control is not needed. (d) open well design of chamber consists 6 coverslips as well as a thick soft silicone chamber sandwiched between two rigid steel plates. Two needles are placed in each well one for aspirating liquid and another for adding and removing liquid. Open Chamber allows for liquid exchange rates higher than closed systems and the multi well format allows for simultaneous imaging and hybridization.

Extended Figure 6: Dataset. Visualization of 400 sections collected across 15 animals spannind three genetic backgrounds[B6 Male in orange, B6 Female in purple and BTBR Male in Cyan] ordered anterior to posterior.

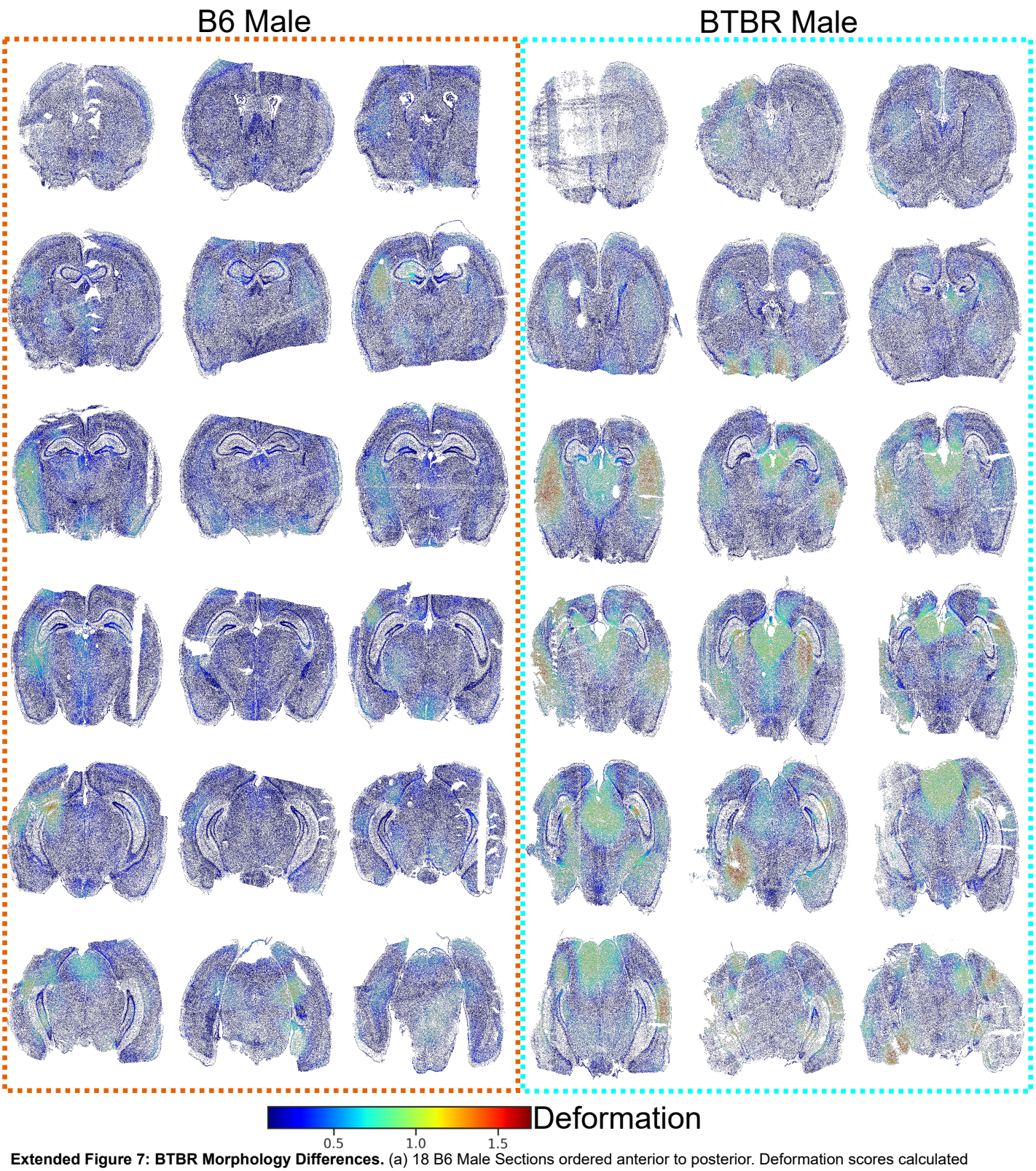

Extended Figure 7: BTBR Morphology Differences. (a) 18 B6 Male Sections ordered anterior to posterior. Deformation scores calculated as the absolute fold change in density for each cell before and after registration to common coordiante framework. (b) 18 BTBR Male Sections. known morphological changes in BTBR including loss of corpus callosum and and a severely reduced hippocampal commisure show high deformation scores compared to the relatively low deformation scores in B6 mice.